https://doi.org/10.5194/egusphere-2023-2215
Preprint. Discussion started: 17 October 2023

Can $\Delta^{14}CO_2$ observations help atmospheric inversions constrain the fossil CO_2 emission budget of Europe?

Carlos Gómez-Ortiz[1], Guillaume Monteil[1], Sourish Basu[2,3], and Marko Scholze[1]

[1]Department of Physical Geography and Ecosystem Science, Lund University, Lund, Sweden
[2]Global Modeling and Assimilation Office, NASA Goddard Space Flight Center, Greenbelt, MD, USA
[3]Earth System Science Interdisciplinary Center, University of Maryland, College Park, MD, USA

Correspondence: Carlos Gómez-Ortiz (carlos.gomez@nateko.lu.se)

Abstract. Independent estimation and verification of fossil CO_2 emissions on a regional and national scale is crucial to evaluate the fossil CO_2 emissions and reductions reported by countries as part of their nationally determined contributions (NDCs). Top-down methods, such as the assimilation of *in situ* and satellite observations of different tracers (e.g. CO_2, CO, $\Delta^{14}CO_2$, XCO_2), have been increasingly used lately for this purpose. In this paper, we use the Lund University Modular Inversion Algorithm (LUMIA) to estimate fossil CO_2 emissions and natural fluxes by inverting simultaneously *in situ* observations of CO_2 and $\Delta^{14}CO_2$ over Europe. We evaluate the inversion system by performing a series of Observing System Simulation Experiments (OSSEs). We find that in regions with a dense sampling network, such as Western/Central Europe, when we add $\Delta^{14}CO_2$ observations in an experiment where the prior fossil CO_2 and biosphere fluxes are set to zero, LUMIA is capable of recovering the time series of both categories, reducing the prior to truth root mean square error (RMSE) from 1.26 TgC day^{-1} to 0.12 TgC day^{-1} in fossil CO_2 and from 0.97 TgC day^{-1} to 0.17 TgC day^{-1} in biosphere, and the true total CO_2 budget in 91%. In a second set of experiments, using realistic prior fluxes, we find that, in addition to retrieving the time series of the optimized fluxes, we are able to recover the true regional fossil CO_2 budget in Western/Central Europe by 95% and in Germany by 97%. In regions with low sampling coverage, such as Southern Europe and the British Isles, the posterior fossil CO_2 emissions are not well resolved in any scenario, and the biosphere fluxes can follow the seasonality with a significant bias that makes it impossible to close the total CO_2 budget. We find that the prior uncertainty of fossil CO_2 emissions does not significantly impact the posterior estimates, showing similar results in regions with good sampling coverage like Western/Central and Northern Europe. Finally, it is important to have a good prior estimate of the terrestrial isotopic disequilibrium to avoid including additional noise to the posterior fossil CO_2 fluxes.

1 Introduction

Carbon dioxide (CO_2) emissions from fossil fuels and cement production became the dominant source of anthropogenic emissions to the atmosphere from around 1950, leading to a concentration of CO_2 in the atmosphere of 419.70 ppm on September 16th, 2023, 49% above pre-industrial levels (https://gml.noaa.gov/ccgg/trends/gl_trend.html, accessed September 18th, 2023). Although land and ocean sinks of CO_2 have increased over the past six decades, the fraction of emissions removed from the atmosphere is expected to decline as the CO_2 concentration increases; therefore, a higher proportion of emitted CO_2 will remain

https://doi.org/10.5194/egusphere-2023-2215
Preprint. Discussion started: 17 October 2023

in the atmosphere (Eyring et al., 2021). Monitoring the CO_2 emissions and removals is important to follow compliance with international treaties such as the Paris Agreement (UNFCCC, 2016). In the Agreement, the Parties have committed to report their emissions and removals of CO_2 and other greenhouse gases (GHGs) to the United Nations Framework Convention on Climate Change (UNFCCC) through the annual GHG inventories. In the case of fossil CO_2 emissions, these inventories have been reported to have uncertainties between 5% and 10% in developed countries, and commonly used spatialized emission inventories such as EDGAR (Emissions Database for Global Atmospheric Research) report a global uncertainty of approximately 11% (Solazzo et al., 2021). However, uncertainties in estimating fossil CO_2 emissions could be more significant and challenging to characterize at sub-annual and sub-national scales, even in developed countries (Basu et al., 2016; Miller et al., 2012; Han et al., 2020).

Constraining fossil CO_2 emissions to sub-annual and sub-national scales is important to improve the accuracy of the GHG inventories. One way of performing this constraint is using atmospheric observations of CO_2 to improve the knowledge on the fossil CO_2 fluxes, known as well as inverse modeling. So far, atmospheric CO_2 inversion frameworks have predominantly been used to constrain terrestrial sources and sinks of CO_2 (Basu et al., 2013; Chevallier et al., 2007; Monteil et al., 2020; Monteil and Scholze, 2021). To constrain the terrestrial carbon cycle, inverse modelers usually prescribe fossil CO_2 fluxes from emission inventories, assuming to be perfectly well-known, to avoid any bias in the fossil CO_2 flux influence the estimates of the biosphere flux (Turnbull et al., 2009). CO_2 atmospheric concentrations represent a mixture of all sources, where the biosphere signal is predominant during most of the year (growing season covering spring to fall), masking the contribution of fossil CO_2 emissions (Shiga et al., 2014). This means that additional information is necessary to separate the fossil apportionment from the natural signal in CO_2 atmospheric observations to be able to constrain the fossil CO_2 fluxes. Some attempts have included sampling strategies where the observations are taken close to the largest fossil CO_2 sources (e.g. cities and power plants) (Bréon et al., 2015) or satellite observations of large point sources such as column-integrated atmospheric CO_2 concentration (XCO_2) (Kaminski et al., 2022; Wang et al., 2020). A more commonly used approach is to combine these CO_2-only observations (either CO_2 or XCO_2) with additional tracers such as NO_2 and the NO_x:CO_2 ratio (Kuhlmann et al., 2021), or ground observations of CO (Newman et al., 2013; Brioude et al., 2013), APO (Atmospheric Potential Oxygen) (Pickers et al., 2022), and more widely the radiocarbon ($\Delta^{14}CO_2$) content of carbon dioxide (Turnbull et al., 2009; Basu et al., 2016; Wang et al., 2018) that we use in this study.

Radiocarbon is the radioactive isotope of carbon with a half-life time of ∼5730 years and is produced naturally in the upper atmosphere by cosmic-ray-induced reactions with nitrogen (Turnbull et al., 2009). Fossil CO_2 does not contain radiocarbon (it has already decayed), and adding its ^{14}C-free emissions to the atmosphere causes a depletion of $\Delta^{14}CO_2$ (Suess, 1955). Meanwhile, radiocarbon is being absorbed and released by the ocean and the biosphere, making it a good tracer of the natural carbon cycle and, therefore, a tool to distinguish fossil emissions from this natural cycle signal in atmospheric CO_2 observations (Turnbull et al., 2009, 2022; Zazzeri et al., 2023). Radiocarbon is also produced as a by-product of nuclear facilities (e.g. nuclear power plants) and atmospheric nuclear weapon tests, the latter mostly between 1945 and 1980 (with the highest intensity in 1961-1962) (Naegler and Levin, 2006). These bomb tests caused a large disturbance in the radiocarbon cycling, resulting in a biosphere and ocean isotopic disequilibrium. Isotopic disequilibrium is the difference between isotopic signatures or

https://doi.org/10.5194/egusphere-2023-2215
Preprint. Discussion started: 17 October 2023

radiocarbon content of carbon entering and leaving a pool. Despite its similar meaning, this occurs differently in the ocean and the biosphere. In the ocean, the disequilibrium results from Δ^{14}C-depleted CO_2 from water that returned to the surface and was out of contact with the atmosphere, so the radiocarbon has decayed significantly. In the biosphere, the disequilibrium results from the heterotrophic respiration of Δ^{14}C-enriched CO_2 assimilated a couple of decades ago when the atmospheric Δ^{14}C was higher due to the bomb spike (Lehman et al., 2013). Therefore, the ocean disequilibrium flux tends to dilute the atmospheric Δ^{14}C content, whereas the biosphere disequilibrium flux tends to enrich it.

The usefulness of atmospheric $\Delta^{14}CO_2$ observations to estimate the fossil CO_2 in the atmosphere as a fraction of the total atmospheric CO_2 concentration has already been demonstrated in various modeling studies (Levin and Karstens, 2007; Turnbull et al., 2009; Vardag et al., 2015). Nevertheless, inversion systems have only recently included $\Delta^{14}CO_2$ as an additional tracer to constrain fossil CO_2 emissions (Basu et al., 2016, 2020; Wang et al., 2018). Results from Observing System Simulation Experiments (OSSE) based on synthetic observations, assuming the current as well as an anticipated future network of $\Delta^{14}CO_2$ measurement stations, have shown the high potential of constraining fossil CO_2 emissions over North America (Basu et al., 2016, 2020) and Europe (Wang et al., 2018). Having a network of both CO_2 and $\Delta^{14}CO_2$ measurement stations requires significant investments to guarantee long monitoring periods that allow the identification of the sub-annual and sub-national scale variations in fossil CO_2 emissions. In Europe, the Integrated Carbon Observation System (ICOS) atmospheric network includes 39 stations in 14 European countries and overseas territories. Hourly CO_2 atmospheric observations are available for 26 stations, with the earliest data from 2015 when the network was created. However, some of these stations already existed by then, and there is information from previous years. Fourteen stations measure $\Delta^{14}CO_2$ in 2-weekly integrated samples analyzed by the ICOS Central Radiocarbon Laboratory. The ICOS network is expanding to include more stations, and new sampling strategies are being developed to increase the number of $\Delta^{14}CO_2$ measurements.

In this work, we explore the interest of using these observations to constrain the fossil CO_2 emissions in Europe. For this, we expanded the LUMIA system (Monteil and Scholze, 2021) to perform simultaneous inversions of atmospheric CO_2 and $\Delta^{14}CO_2$, thus optimizing the fossil emissions, natural fluxes, and the isotopic disequilibrium. We perform observing system simulation experiments (OSSEs), recreating the current state of the ICOS network and its sampling strategy, and using different flux products (as priors and true values) to demonstrate the performance of the inversion scheme and show its capabilities.

2 Theoretical background

The depletion of radiocarbon in the atmosphere due to fossil CO_2 emissions has been demonstrated in various studies since the 1950s, mainly from Δ^{14}C content in tree rings (Suess, 1955; Tans et al., 1979). Anthropogenic disturbances in the atmospheric radiocarbon content, such as the nuclear bomb tests and the nuclear power facilities (Hesshaimer and Levin, 2000), led to the study and better understanding of the radiocarbon exchange between the atmosphere and the biosphere (Hahn et al., 2006) and the ocean (Hesshaimer et al., 1994).

With later improvements in the measurement and modeling techniques, $\Delta^{14}CO_2$ observations were used to estimate the fossil CO_2 offset in atmospheric CO_2 (Levin and Hesshaimer, 2000; Kuc et al., 2003; Naegler and Levin, 2006; Levin and

https://doi.org/10.5194/egusphere-2023-2215
Preprint. Discussion started: 17 October 2023

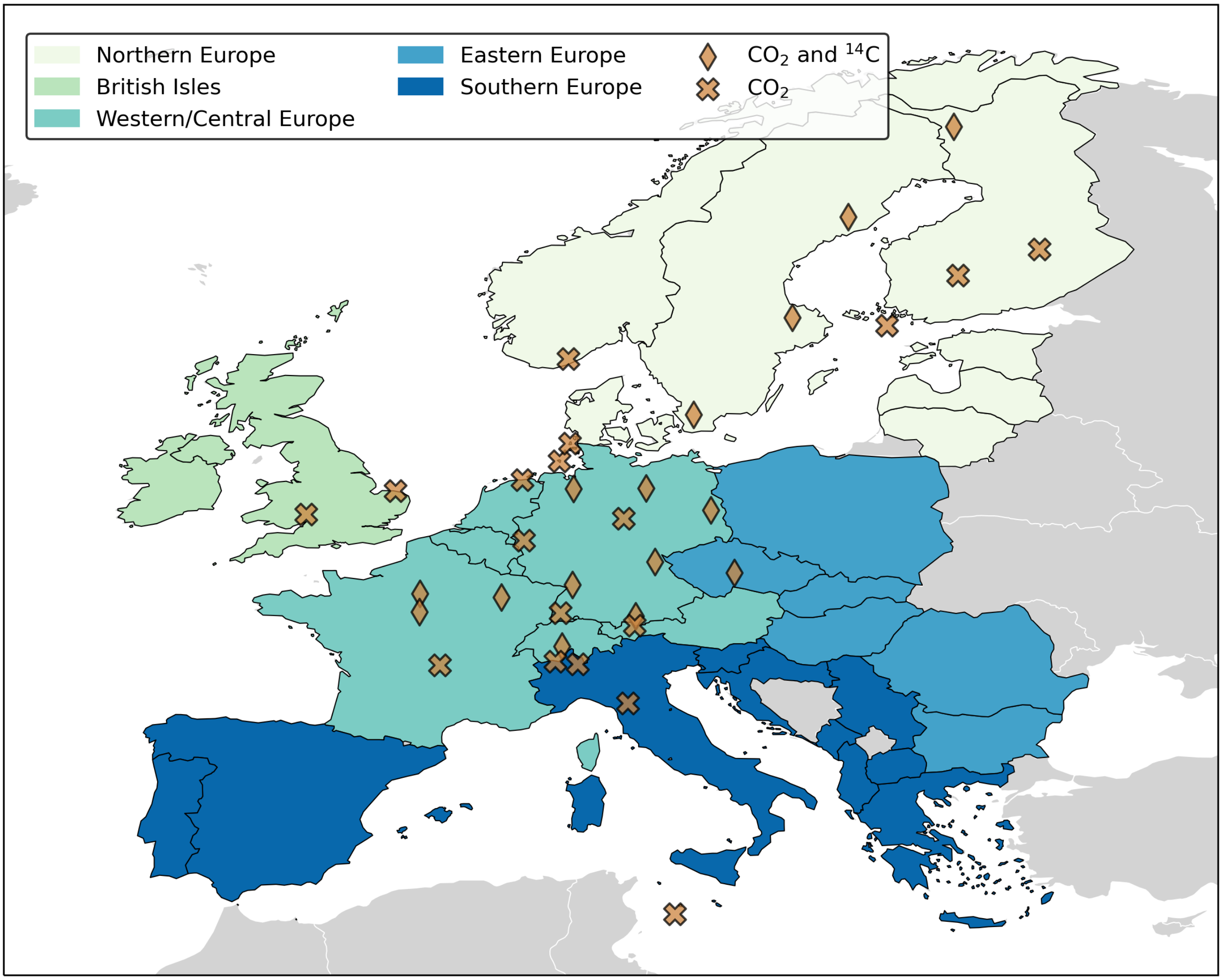

Figure 1. Study domain and location of the ICOS Atmosphere network sampling stations used in this paper. The regions will be used for the analysis and discussion of the results.

Karstens, 2007; Levin et al., 2008) by comparing observations from free troposphere background stations against regional polluted stations, becoming an important precursor for estimating fossil CO_2 emissions using inverse modeling as we describe
95 in the following sections.

2.1 Regional transport model

We perform the inversions for a regional domain ranging from 15°W, 33°N to 35°E, 73°N (depicted in Figure 1, corresponding to the one used in previous studies, e.g. Monteil et al. (2020) and Thompson et al. (2020)).

https://doi.org/10.5194/egusphere-2023-2215
Preprint. Discussion started: 17 October 2023

The link between the surface C fluxes and the CO_2 and $\Delta^{14}CO_2$ concentrations, following the implementation of Rödenbeck et al. (2009), is defined as:

$$y^i_{CO_2} = y^i_{bg[CO_2]} + \sum_c H(F_c) \tag{1a}$$

$$y^i_{C\Delta^{14}C} = y^i_{bg[C\Delta^{14}C]} + \sum_c H(\Delta_c F_c) \tag{1b}$$

where y^i is the modeled concentration corresponding to the observation i, y^i_{bg} is the modeled background concentration (i.e. boundary condition). The operator H represents the regional transport model (see Section 3.2), which is used to calculate the contribution of surface fluxes F (in each category c) to the change of CO_2 and $\Delta^{14}CO_2$ in the atmosphere. F_c in this study corresponds to gridded fluxes in a resolution of 0.5° × 0.5° and 1-hourly. In Eq. 1b, the term Δ_c refers to the $\Delta^{14}CO_2$ signature of the accompanying flux category (Tans et al., 1979; Turnbull et al., 2016). Since $\Delta^{14}CO_2$ ‰ values are not additive and following Basu et al. (2016), we convert all values to $CO_2\Delta^{14}CO_2$ values (or $C\Delta^{14}C$ for simplification). This means that we do not model $\Delta^{14}CO_2$ in ‰ (permil) units, as reported in observations ($\Delta^{14}CO_2$), but in units of amount of $CO_2 \times$ ‰ (e.g. CO_2 ppm‰ for concentrations, PgC‰ yr^{-1} for fluxes). $\Delta^{14}CO_2$ ‰ is the enrichment of depletion of the atmosphere relative to a standard (Stuiver and Polach, 1977), that in this case, is the amount of radiocarbon relative to an absolute standard of ^{14}C from 1950 (Trumbore et al., 2016), meaning that positive values indicate that the ^{14}C content in the sample is higher than the pre-industrial atmosphere.

Expanding the foreground part of Equation 1 to include the flux categories yields explicitly

$$\sum_c H(F_c) = H(F_{ff}) + H(F_{bio}) + H(F_{oce}) \tag{2a}$$

where F_{ff} is the fossil CO_2 emissions, F_{bio} is the net CO_2 flux between the atmosphere and the terrestrial ecosystems (Net Ecosystem Exchange, NEE, in the following also called biosphere flux), and F_{oce} is the atmosphere-ocean CO_2 exchanges. The reason to calculate each $H(F_c)$ is to keep track of the influence of each category and not just the total. For radiocarbon, the equation looks similar but includes an additional term for the radiocarbon from nuclear facilities:

$$\sum_c H(\Delta_c F_c) = H(\Delta_{ff} F_{ff}) + H(\Delta_{atm}(F_{bio} + F_{oce})) + H(F_{bio2atm}(\Delta_{bio} - \Delta_{atm})) + H(F_{oce2atm}(\Delta_{oce} - \Delta_{atm})) + H(\Delta_{nuc} F_{nuc}) \tag{2b}$$

$$= H(\Delta_{ff} F_{ff}) + H(\Delta_{atm}(F_{bio} + F_{oce})) + H(F_{biodis}) + H(F_{ocedis}) + H(\Delta_{nuc} F_{nuc}) \tag{2c}$$

(2d)

where Δ_{ff} is set equal to -1000‰, indicating that fossil CO_2 does not contain any $\Delta^{14}CO_2$ and, therefore, the fossil CO_2 emissions will dilute the atmospheric $\Delta^{14}CO_2$ content. $\Delta_{atm} F_{bio}$ and $\Delta_{atm} F_{oce}$ refer to the exchange of "modern" $C\Delta^{14}C$

https://doi.org/10.5194/egusphere-2023-2215
Preprint. Discussion started: 17 October 2023

between the terrestrial ecosystems and the ocean, respectively, with the atmosphere since Δ^{14}C in new biomass and the top ocean would be nearly the same as atmospheric Δ^{14}C (Δ_{atm}) (Graven et al., 2020). F_{biodis} and F_{ocedis} correspond to the isotopic disequilibrium or the isotopic difference between the source (ocean or biosphere) and the atmosphere. F_{biodis} is the "old-captured" and Δ^{14}C-enriched CΔ^{14}C released through heterotrophic respiration (F_{bio2atm}). F_{ocedis} is the "old-captured" and Δ^{14}C-depleted CΔ^{14}C released through vertical transport of water masses (F_{oce2atm}) (Lehman et al., 2013; Basu et al., 2016). F_{nuc} is the radiocarbon production due to the nuclear activities, mainly from nuclear facilities, since radiocarbon production from nuclear bomb tests has been depleted nowadays (Hesshaimer and Levin, 2000). Converting $\Delta_{\text{nuc}} F_{\text{nuc}}$ to CΔ^{14}C notation, to put it in modeling units as mentioned above, yields:

$$\Delta_{\text{nuc}} F_{\text{nuc}} = \frac{N}{r_{\text{std}}} F_{\text{nuc}} \tag{3}$$

where r_{std} is the ^{14}C : C standard ratio (1.176×10^{-12}) and $N = (975/(\delta^{13}C + 1000))^2$ the isotope fractionation correction (Basu et al., 2016; Stuiver and Polach, 1977). Combining equations 1 through 3 yields for the modeled CO_2 and $\Delta^{14}CO_2$ concentrations:

$$y^i_{\text{CO}_2} = y^i_{\text{bg[CO}_2]} + H(F_{\text{ff}}) + H(F_{\text{bio}}) + H(F_{\text{oce}}) \tag{4a}$$

$$y^i_{\text{C}\Delta^{14}\text{C}} = y^i_{\text{bg[C}\Delta^{14}\text{C]}} + H(\Delta_{\text{ff}} F_{\text{ff}}) + H(F_{\text{biodis}}) + H(F_{\text{ocedis}}) + H(\Delta_{atm}(F_{\text{bio}} + F_{\text{oce}})) + H(\frac{N}{r_{\text{std}}} F_{\text{nuc}}) \tag{4b}$$

There is an additional source of radiocarbon that is not included in Equation 4: the cosmogenic production. This cosmogenic radiocarbon production occurs naturally in the upper atmosphere due to cosmic-ray-induced reactions with nitrogen. This term is implicitly included in the background $y^i_{\text{bg[C}\Delta^{14}\text{C]}}$.

2.2 Observations

The sampling stations shown in Figure 1 depict the ICOS Atmosphere network for 2018-2020 (new sampling stations have been added since then). The ICOS Atmosphere network is part of ICOS, a European research infrastructure that aims to provide long-term, high-quality, and harmonized carbon observations. The Atmosphere network comprises 33 stations distributed across Europe, all measuring CO_2, and 15 stations additionally measuring $\Delta^{14}CO_2$. Two sampling strategies are implemented at the ICOS stations: continuous and periodical sampling. Continuous sampling is made in almost every sampling height available in the station, using commercially available automatic samplers to take hourly measurements of e.g. CO_2. Periodical sampling is made using flask samplers only at the highest sampling height. The flasks are subsequently analyzed at the different ICOS laboratories. There are 1-hour integrated flask samples taken every three days that are used for quality control of the continuous sampling, but as well for measuring other gases that are not measured continuously (e.g. SF_6, H_2, stable isotopes of CO_2), and Δ^{14}C for determining the atmospheric fossil CO_2 component through inverse modeling (Levin et al., 2020). An additional

https://doi.org/10.5194/egusphere-2023-2215
Preprint. Discussion started: 17 October 2023

2-week integrated flask sample passes the air over a solution of NaOH dedicated to $\Delta^{14}C$ sampling. In this paper, we use the 1-hour CO_2 continuous and the 2-week integrated $\Delta^{14}C$ periodical sampling strategies for evaluating LUMIA. A summary of the stations, their location, sampling height, number and average measurements, and integration days is shown in Table 1.

2.3 Inverse modeling problem

Atmospheric inverse modeling can be used for a variety of purposes, including the establishment of the initial conditions of a model, the identification of sources and sinks, and the evaluation and improvement of emission inventories (Bocquet et al., 2015). The goal is to estimate the best set of variables (fluxes) consistent with atmospheric measurements of a tracer (e.g. CO_2 and $\Delta^{14}CO_2$) in the study domain (observations), given the atmospheric transport that relates the two. In its most basic form, this can be formulated as

$$y = H(x,b) + \epsilon \tag{5}$$

where the control vector x contains the variables (carbon fluxes, F_c) to be estimated, and the observation vector y contains the observations (atmospheric concentrations). H is the observation operator, which includes the transport model and any additional observations processing, such as accounting for the boundary conditions and variables, b, that we will not optimize. ϵ is the error vector that includes the errors in the observations, the transport model, and the control vector.

There are multiple approaches to solving the inverse modeling problem. In this paper, and in general in LUMIA, we use the variational approach, in which the control vector x that minimizes the cost function in Eq. 6 is sought iteratively by minimizing the misfit between the model outputs and the observations that are available over a range of times, also known assimilation window (Chatterjee and Michalak, 2013; Rayner et al., 2019; Scholze et al., 2017):

$$J(x) = \frac{1}{2}(x - x_b)^T B^{-1}(x - x_b) + \frac{1}{2}(Hx - y)^T R^{-1}(Hx - y) \tag{6}$$

where B is the prior uncertainty covariance matrix, and R is the observational uncertainty covariance matrix, controlling the weight of each observation and target variable in the optimization. The iterative procedure searches for the value of x that minimizes $J(x)$, i.e. the value of x for which the gradient $(\nabla_x J)$ is equal to zero. The observation operator $H(x)$ can be expressed as the Jacobian matrix Hx that stores the sensitivity of each observation to each control vector element (Monteil and Scholze, 2021).

2.3.1 Construction of the control vector (x)

The control vector x contains the set of parameters adjustable by the inversion, which are offsets to the different sources and sinks of CO_2 and $\Delta^{14}CO_2$ that we want to estimate. From Equation 4, our main interest is to optimize the fossil CO_2 flux F_{ff}. But, since through the radiocarbon cycle, we can separate the fossil and the natural CO_2, we also need to optimize the fluxes from the biosphere (F_{bio}), as well as the isotopic disequilibrium F_{biodis}, to reduce the uncertainty from these two terms that can

https://doi.org/10.5194/egusphere-2023-2215
Preprint. Discussion started: 17 October 2023

Table 1. Observation stations used in the study. As an example, we include a summary of the number of observations (N_{obs}), average observations ± one standard deviation, and the integration time of $\Delta^{14}CO_2$ samples for the year 2018, according to the data available through the ICOS Python API (https://pypi.org/project/icoscp/, accessed February 2023). Stations with zero N_{obs} did not measure or report observations of the corresponding tracer in 2018 to ICOS, but we include them in this study.

Code	Name	Country	Lat (°E)	Lon (°N)	Altitude (m.a.s.l)	Max. samp. height (m.a.g.l)	N_{obs} CO_2	N_{obs} $\Delta^{14}C$	Avg. CO_2 (ppm)	Avg. $\Delta^{14}C$ (‰)	Integration time (days)
BIR	Birkenes	NO	58.39	8.25	219	75	2616	–	421.9 ± 8.0	–	–
CMN	Monte Cimone	IT	44.19	10.70	2165	8	5832	–	406.3 ± 6.0	–	–
GAT	Gartow	DE	53.07	11.44	70	341	8784	0	419.5 ± 10.0	–	–
HEL	Helgoland	DE	54.18	7.88	43	110	1080	–	430.4 ± 10.1	–	–
HPB	Hohenpeissenberg	DE	47.8	11.02	934	131	8784	17	415.6 ± 6.8	-4.1 ± 2.8	13.4 ± 0.5
HTM	Hyltemossa	SE	56.1	13.42	115	150	8784	21	417.1 ± 8.4	-3.2 ± 3.2	14.0 ± 1.6
IPR	Ispra	IT	45.81	8.64	210	100	8784	–	430.0 ± 15.9	–	–
JFJ	Jungfraujoch	CH	46.55	7.99	3580	5	8784	15	413.1 ± 3.6	-1.0 ± 3.5	14.0 ± 0.0
JUE	Jülich	DE	50.91	6.41	98	120	8784	–	423.0 ± 11.2	–	–
KIT	Karlsruhe	DE	49.09	8.42	110	200	8784	21	428.7 ± 17.5	-14.1 ± 10.4	6.2 ± 0.7
KRE	Křešín u Pacova	CZ	49.57	15.08	534	250	8784	13	422.0 ± 11.5	-4.1 ± 3.0	13.2 ± 0.6
LIN	Lindenberg	DE	52.17	14.12	73	98	8784	5	426.0 ± 13.1	-8.6 ± 6.3	14.0 ± 0.0
LMP	Lampedusa	IT	35.52	12.63	45	8	8088	–	414.7 ± 4.2	–	–
LUT	Lutjewad	NL	53.4	6.35	1	60	8784	–	422.3 ± 12.2	–	–
NOR	Norunda	SE	60.09	17.48	46	100	8784	19	417.8 ± 8.2	-0.7 ± 4.2	13.3 ± 0.5
OPE	Observatoire pérenne de l'environnement	FR	48.56	5.5	390	120	8784	17	420.2 ± 9.5	-3.3 ± 3.5	13.5 ± 0.5
OXK	Ochsenkopf	DE	50.03	11.81	1022	163	8784	0	416.8 ± 6.4	–	–
PAL	Pallas	FI	67.97	24.12	565	12	8784	17	416.2 ± 7.7	-1.5 ± 3.5	12.9 ± 1.9
PRS	Plateau Rosa	IT	45.93	7.70	3480	10	0	–	–	–	–
PUI	Puijo	FI	62.91	27.65	232	84	1248	–	426.6 ± 4.5	–	–
PUY	Puy de Dôme	FR	45.77	2.97	1465	10	8784	–	414.0 ± 5.4	–	–
RGL	Ridge Hill	GB	52.0	-2.54	199	90	8784	–	413.4 ± 6.1	–	–
SAC	Saclay	FR	48.72	2.14	160	100	8784	12	420.5 ± 10.5	-2.7 ± 6.4	16.5 ± 4.3
SMR	Hyytiälä	FI	61.85	24.29	181	125	8784	–	416.8 ± 8.5	–	–
SSL	Schauinsland	DE	47.92	7.92	1205	35	0	–	–	–	–
STE	Steinkimmen	DE	53.04	8.46	29	252	8784	13	421.9 ± 11.5	-6.7 ± 4.2	13.5 ± 1.6
SVB	Svartberget	SE	64.26	19.77	269	150	8784	13	416.1 ± 8.0	-0.9 ± 3.1	15.6 ± 1.9
TOH	Torfhaus	DE	51.81	10.54	801	147	8784	–	417.6 ± 7.8	–	–
TRN	Trainou	FR	47.96	2.11	131	180	8784	11	419.4 ± 8.6	-4.7 ± 4.8	14.7 ± 3.3
UTO	Utö - Baltic sea	FI	59.78	21.37	8	57	8784	–	416.2 ± 8.0	–	–
WAO	Weybourne	GB	52.95	1.12	31	10	8784	–	413.4 ± 6.1	–	–
WES	Westerland	DE	54.92	8.31	12	14	8784	–	416.2 ± 2.7	–	–
ZSF	Zugspitze	DE	47.42	10.98	2666	3	0	–	–	–	–

https://doi.org/10.5194/egusphere-2023-2215
Preprint. Discussion started: 17 October 2023

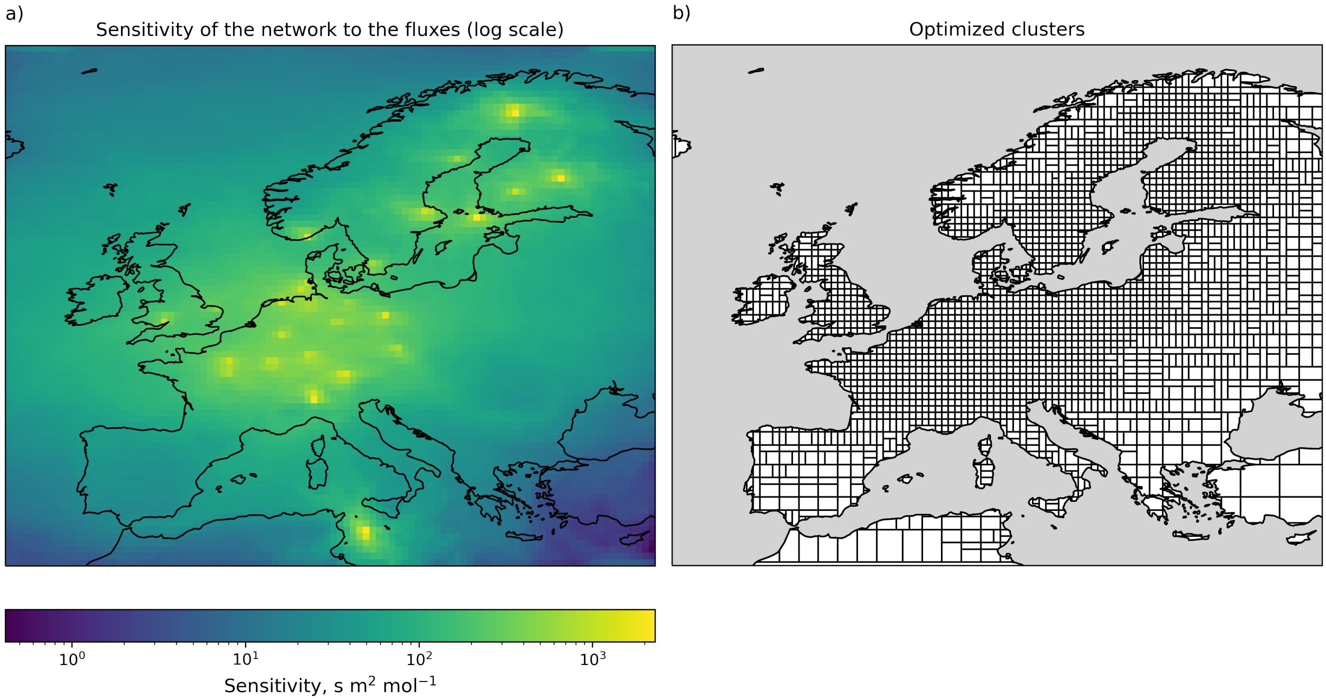

Figure 2. Visual representation of a) the sensitivity of the observation network to each grid-cell (in logarithmic scale) and b) the optimized clusters and their variable spatial resolution.

have an important impact on the inversion result. The remaining fluxes (F_{nuc}, F_{oce}, and F_{ocedis}) are prescribed and not included in the control vector.

In order to limit the computational requirements, we do not solve directly for the high-resolution fluxes (e.g. 0.5° × 0.5° and 1-hourly) used in the transport model, but for weekly offsets for 2500 clusters of grid points. Appendix B describes the clustering algorithm in further detail. In short, it groups together contiguous grid cells, depending on how sensitive the observation network is to their emissions: grid cells directly upwind of the sampling stations are optimized at the native resolution of 0.5°, but in parts of the domain not well sampled by the observations (e.g. North Africa, Turkey), the resolution drops down to 5° × 3.5° (see Figure 2).

The relation between the control vector and the gridded emissions is given by:

$$F_c = F_c^0 + \mathbf{T}_T \mathbf{X}_x^c \mathbf{T}_H \tag{7}$$

where F_c is the vector containing gridded emissions for the category c, with prior value F_c^0. The matrix $\mathbf{X}_x^c$ is the portion of the control vector x that contains offsets for the category c, reshaped as a (n_{opt}^t, n_{opt}^p) matrix, with n_{opt}^t and n_{opt}^p the number of optimized (weekly) time steps and grid-cell clusters, respectively. The matrices $\mathbf{T}_t$ (n_{mod}^t, n_{opt}^t) and $\mathbf{T}_H$ (n_{opt}^p, n_{mod}^p) contain

https://doi.org/10.5194/egusphere-2023-2215
Preprint. Discussion started: 17 October 2023

the relative contribution of each model time step t_{mod} (1 hour) and of each grid-cell p_{mod} (0.5° × 0.5°) to each optimized time-step t_{opt} and cluster p_{mod}.

2.3.2 Construction of the prior error covariance matrix (B)

Since we are optimizing for offsets, the prior control vector x_b contains only zeros (so $F_c = F_c^0$). The uncertainties on x_b are given by the error covariance matrix $\mathbf{B}$. We assume no correlation between different categories and different tracers. Therefore, the sections of $\mathbf{B}$ specific to each tracer/category can be constructed independently. We do this in three steps:

1. Construct a vector of variances (diagonals of $\mathbf{B}$), which contain the spatio-temporal pattern of the uncertainties.

2. Construct the covariances based on spatial and temporal correlation functions. Specifically, the covariances are set following $cov(x_1, x_2) = \sigma_{x_1}\sigma_{x_2}e^{-(d(p1,p2)/L_h)^2}e^{-|t2-t1|/L_t}$, with $d(p1,p2)$ the geographical distance between the center of the clusters (area-weighted average of the center-coordinates of the grid-cells in the cluster), and $|t2-t1|$ the temporal distance between x_1 and x_2.

3. Scale the entire (section of the) $\mathbf{B}$ matrix by a uniform scaling factor to match a prescribed category-specific annual uncertainty value δF_c.

The values of correlation lengths L_h and L_t, as well as the scaling factors δF_c are provided in Section 3.3.1. For constructing the vector of variances (σ_x^2), two approaches were used:

- For fossil CO_2 emissions F_{ff}, the variance is set to $\sigma^2_{p,t,c} = |\sum_{i,j,t_{mod}} F^c_{i,j,t_{mod}}|^2$, where $\sigma^2_{p,t,c}$ is the variance corresponding to the control vector elements for the time step t and spatial cluster p of category c. The spatial coordinates i and j are the ensemble of grid cells that are within the cluster p, and the temporal coordinate t_{mod} is the ensemble of 1-hourly model time steps that are within the (weekly) optimization time-step t. For instance, if the cluster p groups four model grid-cells, the variance $\sigma^2_{p,t,c}$ will be calculated over 672 flux components (4 grid-cells, seven days with 24 hourly time steps).

- For the other fluxes, the procedure is similar, but the formula is $\sigma^2_{p,t,c} = \sqrt{|\sum_{i,j,t_{mod}} F^c_{i,j,t_{mod}}|}$.

The rationale behind these formulas is to scale the uncertainties to the prior estimate of the fluxes (assuming that very low prior fluxes should imply low prior uncertainties) but avoid artificially low errors in instances where negative and positive fluxes compensate each other (i.e., NEE, in the spring and autumn times). Furthermore, the location of fossil CO_2 emissions is relatively better known. Therefore, the formula used for fossil CO_2 emissions concentrates the uncertainties more at the location of prior emissions than that used for the other categories. Regardless of the formula used for determining the variance, it is scaled afterward to match the target uncertainty reported in Table 2.

https://doi.org/10.5194/egusphere-2023-2215
Preprint. Discussion started: 17 October 2023

3 Observing System Simulation Experiments (OSSEs)

In order to assess the performance of the inversion system, we designed and performed a series of Observing System Simulation Experiments (OSSEs). In so-called OSSEs, the impact of new observing systems, configurations of existing systems, observing strategies, and the optimization of new data are evaluated (Hoffman and Atlas, 2016). This is done by generating a set of simulated observations, called synthetic observations, from a set of reasonable but arbitrary fluxes, $\hat{F}_c$, considered 'true' fluxes in the OSSE. Then, by using fluxes from different models or products as prior fluxes (F_c), we investigate the ability of an inverse modeling system to reconstruct the true fluxes consistent with the model setup (e.g. prescribed uncertainties, error structure). In the following sections, we describe the different data sets, model setups, assumptions, and experiments used in this study.

3.1 True and prior fluxes

We use a set of fluxes commonly used in this kind of inverse problem with a high horizontal and temporal resolution (0.5° × 0.5° and 1 hour, respectively) to generate our synthetic observations. For the CO_2 fluxes, we use EDGARv4.3 emission inventory (Janssens-Maenhout et al., 2019) distributed spatially and temporally based on fuel type, category, and country-specific emissions, using the COFFEE approach (Steinbach et al., 2011) (EDGAR in Table 3, see (Gerbig and Koch, 2021b)) as $\hat{F}_{\text{ff}}$ for the base year 2018. For $\hat{F}_{\text{bio}}$, we use a simulation of the LPJ-GUESS vegetation model (Smith et al., 2014) (LPJ-GUESS in Table 3, see (Wu, 2023)), and for $\hat{F}_{\text{oce}}$, we use the Jena Carbo-Scope v1.5 product (Rödenbeck et al., 2013). We use the terrestrial and ocean disequilibrium and nuclear fluxes from Basu et al. (2020) as our $\hat{F}_{\text{biodis}}$ (BASU in Table 3), $\hat{F}_{\text{ocedis}}$ and $\hat{F}_{\text{nuc}}$, respectively.

As prior fluxes, we use products that followed different methodologies and schemes, with different spatial and temporal structures than the true fluxes, to make the implementation more realistic. For F_{ff}, we use a version of ODIAC (Open-source Data Inventory for Anthropogenic CO_2) (ODIAC in Table 3, see (Oda and Maksyutov, 2020)) with a 1km × 1km spatial and monthly temporal resolution. Thus, our prior fossil CO_2 fluxes include monthly variability but do not resolve the daily cycle (Oda et al., 2018). We also prepare a flat-year average version of this product (FlatODIAC in Table 3). For F_{bio}, we use a product from simulations of the VPRM vegetation model (Mahadevan et al., 2008; Thompson et al., 2020) (VPRM in Table 3, see (Gerbig and Koch, 2021a)). Due to the lack of an alternative product for the F_{biodis}, we generate our own prior by calculating a series of randomly perturbed versions of the true flux following their prescribed uncertainties and their horizontal and temporal correlations (RndBASU in Table 3). This perturbation is done by adding a random perturbation to the control vector and transforming such vector to the flux space. All fluxes are gridded to 0.5° × 0.5° and 1-hour resolution by the nearest neighbor interpolation.

3.2 Observation footprints (FLEXPART)

Similar to Monteil and Scholze (2021), we compute the regional transport (e.g. operator H in Equation 4) using the FLEXPART 10.4 Lagrangian transport model (Pisso et al., 2019). For each observation, FLEXPART computes a "footprint", i.e. a vector

https://doi.org/10.5194/egusphere-2023-2215
Preprint. Discussion started: 17 October 2023

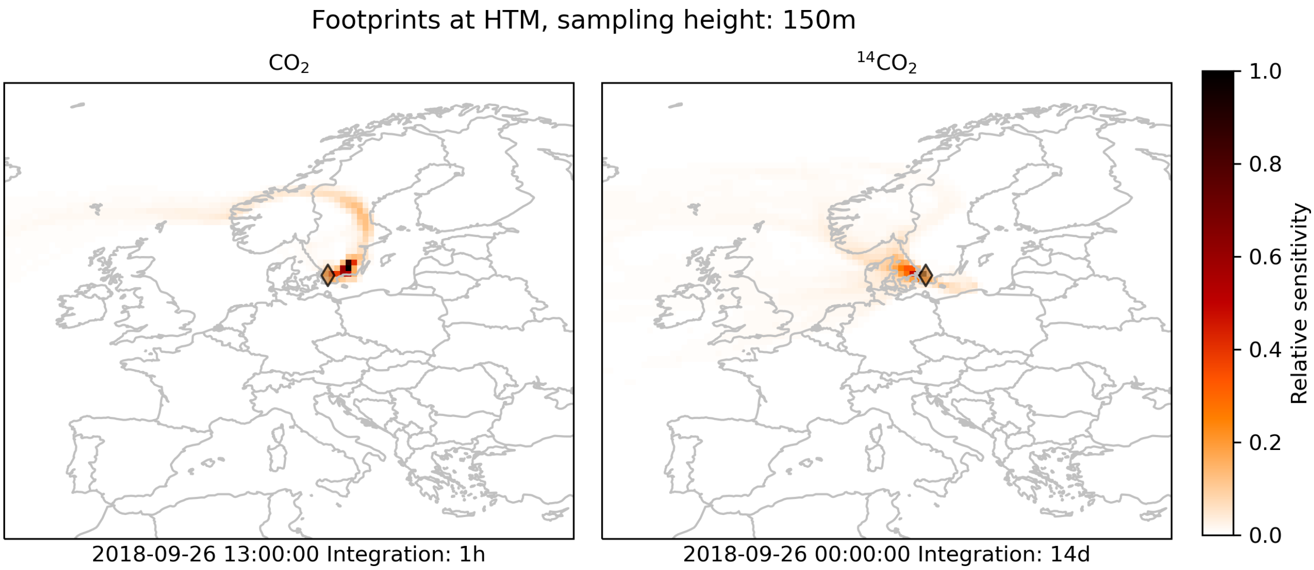

Figure 3. Example of pre-calculated observations footprints for CO_2 (left) and $\Delta^{14}CO_2$ (right) at Hyltemossa station. $\Delta^{14}CO_2$ (right) has an integration time of 14 days.

containing the sensitivity of the observation to changes in the surface fluxes. The footprints are pre-computed and then used throughout the subsequent steps of the inversion (see Monteil and Scholze (2021) for further details). The FLEXPART simulations were driven by ERA5 reanalysis data at a horizontal resolution of $0.5° \times 0.5°$ and 1-hourly temporal resolution. The footprints were computed differently for the CO_2 and $\Delta^{14}CO_2$ observations. For CO_2, we computed a set of footprints for each observation up to 14 days backward in time, following the approach from Monteil and Scholze (2021). Integrated $\Delta^{14}CO_2$ observations (Section 2.2) quantify the $\Delta^{14}C$ value of atmospheric CO_2 over a period of 1 to 3 weeks (see Table 1). We account for this in FLEXPART by distributing the FLEXPART particles release over the whole integration period of the observations. The simulations are then carried on for (up to) 14 days backward in time from the start of the integration period. A Python code was developed to run FLEXPART and post-process the footprints for being used in LUMIA (https://github.com/lumia-dev/runflex). In Figure 3, we show an example of an observation footprint for CO_2 and $\Delta^{14}CO_2$ at the Hyltemossa ICOS station in southern Sweden. The CO_2 footprint (left of Fig. m 3) shows how the observation of June 26th, 2018 at 13:00 LT is sensitive to fluxes from the North Atlantic, passing through Norway, Sweden, and finally from Sweden's East and South coasts close to the Baltic Sea. The $\Delta^{14}CO_2$ aggregated footprint, on the other hand, shows a more spread sensitivity due to the long integration time, collecting fluxes from Southern Norway, Northwestern Europe, and the Baltic.

3.3 Synthetic observations

We generate concentration time series for one year for each of the stations according to the current setup of the ICOS Atmosphere network. For replicating the most realistic conditions of the sampling frequency, we use real sampling and integration

https://doi.org/10.5194/egusphere-2023-2215
Preprint. Discussion started: 17 October 2023

times (in the case of radiocarbon) from the stations, taking for each one the sampling times for 2018. In this way, we account for the sampling gaps and the differences in integration times commonly produced due to calibrations, maintenance, and general operational eventualities. For stations with the number of observations, N_{obs}, equal to zero in Table 1, we set fixed sampling and integration times (14 days). Most of these stations were already in operation in 2018, but some were not yet labeled as ICOS stations (e.g. Schauinsland) or had not implemented and or started the tracer measurement (e.g. $\Delta^{14}C$ at Ochsenkopf).

Following Monteil and Scholze (2021), we select the CO_2 observation times according to the sampling station's elevation to guarantee the model's best representation. For sampling stations located under 1000 m.a.s.l, we select the times when the boundary layer is most likely well developed, from 11:00 to 15:00 LT. For the contrary case, we take the times around midnight, from 22:00 to 2:00 LT, where the boundary layer is most likely below the sampling intake, or in other words, is sampling the free troposphere. This data selection is not strictly necessary for this study since we assume a perfect transport model (the same model is used to generate the synthetic observations and perform the inversions). However, we want to replicate the conditions of a real inversion. We perform a forward run of the model using the true fluxes mentioned in Section 3.1 to calculate the corresponding "true" CO_2 and $C\Delta^{14}C$ concentration time series and then add a random perturbation to the synthetic observations to weaken the assumption of a perfect transport. Figure 4 shows the synthetic CO_2 concentration and $\Delta^{14}CO_2$ time-series and the components of each flux at Hyltemossa station. As mentioned in Section 2.1, we convert all radiocarbon values to $C\Delta^{14}C$ values. On the side of the observation, we do this by applying the following equation:

$$[C\Delta^{14}C] = \frac{[\Delta^{14}CO_2] \times [CO_2]}{1000} \tag{8}$$

In a real setup, this would imply having paired CO_2 and $\Delta^{14}CO_2$ observations, and in the case of the integrated samples, this would mean having an average of CO_2 observations along the integration period of the $\Delta^{14}CO_2$ sample. However, since we are using synthetic observations, we transported the CO_2 fluxes using the $\Delta^{14}CO_2$ footprints and stored the values to convert back and forth between $\Delta^{14}CO_2$ and $C\Delta^{14}C$ units, ‰ and ppm‰, respectively.

As can be seen from Figure 4, both $\hat{F}_{\text{oce}}$ and $\hat{F}_{\text{ocedis}}$ have virtually no impact on the concentrations at the Hyltemossa station (and all other stations used in our setup, not shown), hence we decided not to include these components in the control vector, i.e. we transport them but do not optimize them further.

3.3.1 Experiments and inversion setup

To make the inversions comparable, we keep the same inversion setup for all the experiments. Table 2 summarizes the main model parameter values. We choose a Gaussian horizontal correlation and an exponential temporal correlation for the prior flux uncertainties (See Section 2.3.1). The prior uncertainties are assigned as follows: 50% to 150% (0.1 PgC yr^{-1} to 0.3 PgC yr^{-1}) of the difference in the annual budget (0.21 PgC yr^{-1}) of EDGAR and ODIAC for F_{ff} to evaluate its impact in the inversion, 10% (0.37 PgC yr^{-1}) of the annual negative values for F_{bio} (where production is higher than respiration), and 30% (0.22 PgC yr^{-1}) of the annual budget for F_{biodis}. We optimize all the categories at the same temporal resolution but at a higher horizontal resolution for F_{ff} and F_{bio} (2500 points) than for F_{biodis} (500 points). To set up the observation uncertainty, we use

https://doi.org/10.5194/egusphere-2023-2215
Preprint. Discussion started: 17 October 2023

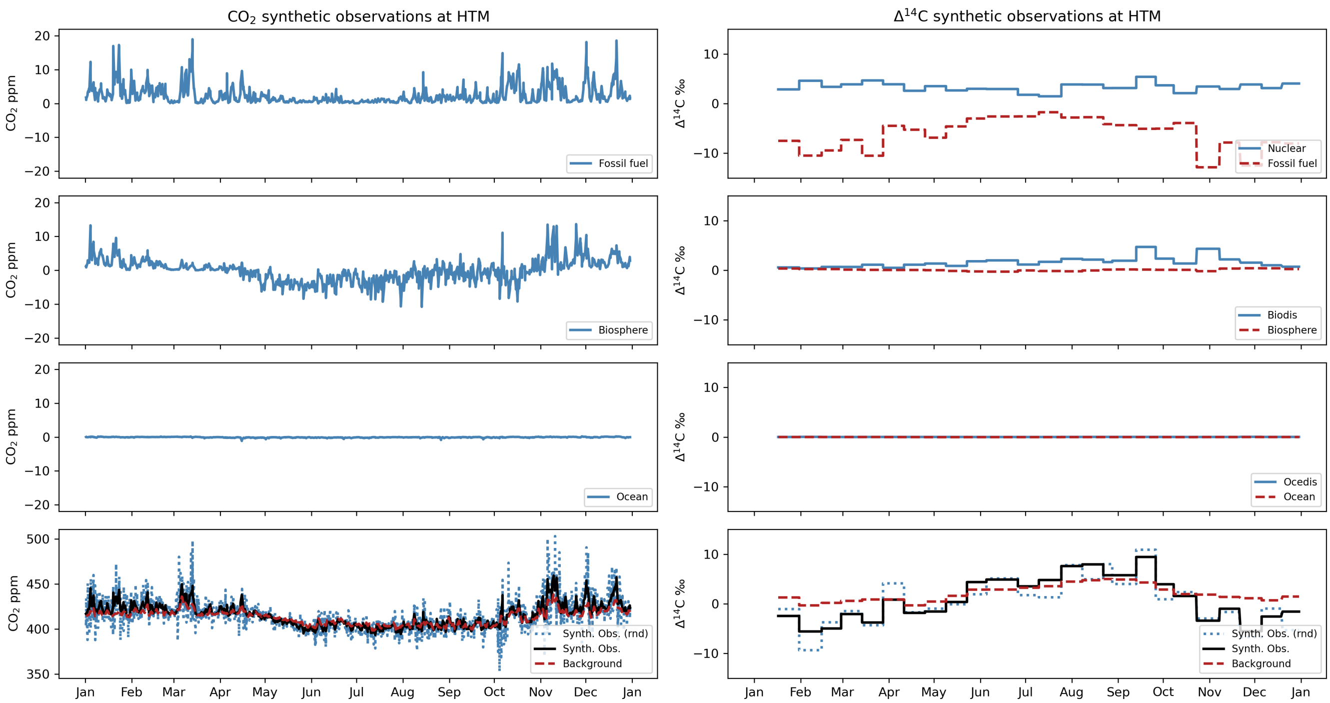

Figure 4. Synthetic observation time-series for Hyltemossa (HTM) station.

different methods for the CO_2 and the $\Delta^{14}CO_2$. For CO_2, we apply a weekly moving standard deviation to each observation i.e. the prior uncertainty of each observation is equal to the standard deviation of the observations in a time window of ± 3.5 days around that observation. The prior uncertainty for the CO_2 observations ranges from 0.91 to 215.5 ppm. For $\Delta^{14}CO_2$, we use a constant value of 1.5‰ for $\Delta^{14}CO_2$.

We perform one forward run and six inversions, summarized in Table 3. We generate the synthetic observations and evaluate the impact of $\hat{F}_{\mathrm{oce}}$ and $\hat{F}_{\mathrm{ocedis}}$ on the total synthetic observations as described in Section 3.3 with the forward run (SYNTH). Starting with the inversions, we perform two experiments to test the impact of having $\Delta^{14}C$ observations (ZBASE and ZCO2Only). We use the prior F_{ff} and F_{bio} set to zero (both in the spatial and temporal domain) with a prior uncertainty setup based on ODIAC and VPRM, respectively. The reason to use prior fluxes set to zero is that products of both categories can have similar spatial and temporal distributions and values, making it easy for the model to retrieve the true values. Instead, we set the values to zero but give the model some information through the prior uncertainty setup. The remaining fluxes are prescribed and set to their true values. We assimilate both CO_2 and $\Delta^{14}C$ observations for ZBASE and only CO_2 observations for ZCO2Only. In the second set of inversions, we use a more realistic setup. In the first, BASE, we simulate a complete and realistic inversion setup, assimilating CO_2 and $\Delta^{14}C$ observations and optimizing F_{ff}, F_{bio}, and F_{biodis}. In the BASE experiments, we change the prescribed prior uncertainty of F_{ff} (0.1, 0.21 and 0.3 PgC yr^{-1}) to evaluate its impact on the optimization. With the last inversion, BASENoBD, we evaluate the impact of the prior F_{biodis} product in the posterior F_{ff}. The terrestrial dis-

https://doi.org/10.5194/egusphere-2023-2215
Preprint. Discussion started: 17 October 2023

Table 2. Parameter setup used in all the inversions performed in this study.

Fluxes						
Flux category	Horizontal correlation	Temporal correlation	Prior uncertainty ($PgC\ yr^{-1}$)	Error structure	Optimization interval (days)	Grid points
F_{ff}	200-g	1-e-monthly	0.30	log	7	2500
F_{bio}	500-g	1-e-monthly	0.37	sqrt	7	2500
F_{biodis}	1000-g	2-e-monthly	0.22	sqrt	7	500
Observations						
		Tracer	Type of sampling	Prior uncertainty		
		CO_2	Continuous 1-hour	Weekly moving standard deviation		
		$\Delta^{14}CO_2$	Integrated 2-weekly	Constant 0.8 ppm ‰		

Table 3. Inversions performed in this work.

Simulation	F_{ff}	F_{bio}	F_{biodis}	Optimized fluxes	Tracers	Run
SYNTH	EDGAR	LPJ-GUESS	BASU	None	CO_2, $\Delta^{14}CO_2$	Forward
ZBASE	ZEROFossil	ZEROBio	BASU	F_{ff}, F_{bio}	CO_2, $\Delta^{14}CO_2$	Inversion
ZCO2Only	ZEROFossil	ZEROBio	BASU	F_{ff}, F_{bio}	CO_2	Inversion
BASE0.1	ODIAC	VPRM	RndBASU	F_{ff}, F_{bio}, F_{biodis}	CO_2, $\Delta^{14}CO_2$	Inversion
BASE	ODIAC	VPRM	RndBASU	F_{ff}, F_{bio}, F_{biodis}	CO_2, $\Delta^{14}CO_2$	Inversion
BASE0.3	ODIAC	VPRM	RndBASU	F_{ff}, F_{bio}, F_{biodis}	CO_2, $\Delta^{14}CO_2$	Inversion
BASENoBD	ODIAC	VPRM	BASU	F_{ff}, F_{bio}	CO_2, $\Delta^{14}CO_2$	Inversion

equilibrium term (F_{biodis}) is difficult to estimate since there is a large uncertainty on the heterotrophic respiration flux and the age of respired carbon (Basu et al., 2016), and it may be widely different if estimated using a different vegetation model or methodology. We account for this by optimizing only the CO_2 fluxes, F_{ff} and F_{bio}, using both CO_2 and $\Delta^{14}C$ observations and keeping $\hat{F}_{biodis}$ prescribed.

https://doi.org/10.5194/egusphere-2023-2215
Preprint. Discussion started: 17 October 2023

4 Results

4.1 Impact of F_{oce} and F_{ocedis}

We start by testing the impact of ocean-related fluxes ($\hat{F}_{\text{oce}}$ and $\hat{F}_{\text{ocedis}}$) in the total synthetic observations by performing a forward simulation (SYNTH in Table 3). Figure 4, shows the results from this forward simulation and the contribution of each flux category to the concentrations of both tracers for the Hyltemossa (HTM) station. The results show that the contribution of the ocean and ocean disequilibrium fluxes to the total concentration is below the error assigned to the synthetic observations. For CO_2, the average contribution is -0.07 ± 0.12 ppm (for an average observation error of 10.0 ± 5.7 ppm) at HTM, -0.07 ± 0.15 ppm (average obs. error 9.8 ± 9.0 CO_2 ppm) at all stations. For $\Delta^{14}CO_2$, the average contribution due to F_{oce} is -0.009 ± 0.009‰ (average obs. error 1.9 ± 0.04‰) at HTM and -0.007 ± 0.007‰ (average obs. error 1.9 ± 0.05‰) at all stations. Similarly, the contribution due to F_{ocedis} is 0.016 ± 0.009‰ at HTM and 0.02 ± 0.017‰ at all stations. Due to the low impact of ocean-related fluxes, we prescribe them in the inversions along with F_{nuc} and optimize only F_{ff}, F_{bio}, and F_{biodis}. A summary for each station can be found in Appendix A.

4.2 Impact of adding Δ^{14}C observations

In this section, we present the results from the ZBASE and ZCO2Only experiments. We start by analyzing the retrieval of truth fossil CO_2 ($\hat{F}_{\text{ff}}$) and biosphere ($\hat{F}_{\text{bio}}$) time series. We divide the results into the regions shown in Figure 1, where Northern Europe represents Scandinavia, Finland, and the Baltic States, Western/Central Europe represents Benelux, France, Germany, Switzerland, Liechtenstein, and Austria, Southern Europe represents the Iberian Peninsula, Italy, and the Balkans (except for Romania and Bulgaria), Eastern Europe represents Poland, Slovakia, Hungary Romania, and Bulgaria, and the British Isles represents Ireland and the United Kingdom. The study domain includes all the land shown in Figure 1, even the countries not mentioned in the definition of the regions (countries in gray in Figure 1).

4.2.1 Retrieval of the monthly and regional time series

The posterior fossil CO_2 (F_{ff}) time series show heterogeneous results across the regions and experiments (Figure 5) in contrast with the biosphere fluxes (F_{bio}), where there is, in general, a good agreement between the truth and the posterior time series for the two experiments in all regions (Figure 6). Starting with the study domain, the posterior ZBASE (adding Δ^{14}C observations) performs better than the ZCO2Only for both flux categories. For F_{ff} (Figure 5a), both experiments show a negative bias and follow the seasonality, albeit ZBASE is closer to the posterior than ZCO2Only and therefore has a lower root mean square error (RMSE): 1.51 TgC day^{-1} versus 2.75 TgC day^{-1}, respectively (see Table 4). Posterior biosphere fluxes, on the other hand, follow the true time series closer than fossil CO_2 in both experiments, with a positive bias (Figure 6a). Once again, ZBASE performs better than ZCO2Only most of the year and presents smaller RMSE (ZBASE = 1.12 TgC day^{-1}, ZCO2Only = 2.12 TgC day^{-1}) and BIAS values (ZBASE = 0.74, ZCO2Only = 1.90) (see Table 4). Before continuing with the regional results, it is important to mention the characteristics of the regions regarding the coverage of the sampling stations. In total,

https://doi.org/10.5194/egusphere-2023-2215
Preprint. Discussion started: 17 October 2023

Table 4. RMSE and BIAS values for F_{ff} and F_{bio} from the ZBASE and ZCO2Only experiments in all the regions.

Region	Fossil fuel (F_{ff})						Biosphere (F_{bio})					
	RMSE (TgC day^-1)			BIAS			RMSE (TgC day^-1)			BIAS		
	Prior	ZBASE	ZCO2Only	Prior	ZBASE	ZCO2Only	Prior	ZBASE	ZCO2Only	Prior	ZBASE	ZCO2Only
Study Domain	4.07	1.51	2.75	-4.03	-1.51	-2.74	4.66	1.12	2.12	1.18	0.74	1.90
Western/Central Europe	1.26	0.12	0.53	-1.25	-0.06	-0.52	0.97	0.17	0.46	0.15	-0.04	0.43
Southern Europe	0.60	0.42	0.51	-0.59	-0.41	-0.50	0.89	0.35	0.41	0.35	0.29	0.35
Eastern Europe	0.55	0.07	0.33	-0.54	-0.02	-0.33	0.61	0.22	0.34	0.15	-0.04	0.26
Northern Europe	0.20	0.19	0.20	-0.20	-0.19	-0.20	0.76	0.21	0.25	0.00	0.16	0.22
British Isles	0.28	0.14	0.15	-0.28	0.07	-0.21	0.30	0.16	0.09	0.02	-0.13	-0.02

we consider 33 stations, all of them measuring CO_2 and 15 measuring additionally $\Delta^{14}C$. Most of the stations are located in Western/Central Europe (18 stations, 10 measuring both tracers), followed by Northern Europe with eight stations, four measuring both tracers, Southern Europe with four stations measuring CO_2 only, the British Isles with two (CO_2) and Eastern Europe with one (CO_2 and $\Delta^{14}C$) (see Figure 1). We find the best posterior time series in Western/Central Europe, which, as we already mentioned, also has the largest number of stations. The posterior fossil CO_2 time series for the ZBASE experiment fit closely with the true time series, while ZCO2Only shows a pronounced bias (Figure 5b) as in the case of the study domain for both experiments. Likewise, the posterior biosphere shows better results when adding $\Delta^{14}C$ observations (ZBASE) than without them (ZCO2Only), in which the latter has a positive bias most of the year (Figure 6b). Eastern Europe and the British Isles show a posterior ZBASE fossil CO_2 close to the truth despite their low coverage of sampling stations. Eastern Europe shows the best results during the year for ZBASE, and ZCO2Only follows the tendency from the last regions (Figure 5d). The British Isles show a posterior ZBASE fossil CO_2 with more differences from the truth, particularly at the beginning of the year, where the posterior surpasses the truth in almost 100% of its value(Figure 5f), resulting in a similar RMSE but a lower BIAS than ZCO2Only (Table 4). However, the posterior ZBASE biosphere fluxes in these two regions do not show a good fit to the truth as in e.g. Western/Central Europe. In Eastern Europe, the posterior ZBASE shows big differences with the truth during May, June (maximum difference of 0.42 TgC day^{-1}), and later in September, while ZCO2Only shows a better fit during these months but a positive bias the rest of the year (Figure 6d). In contrast, the posterior biosphere flux from the ZCO2Only experiment shows a better fit to the truth than the ZBASE one in the British Isles (Table 4). The ZBASE experiment shows a negative bias most of the year, except from March to May (Figure 6f). Lastly, Southern and Northern Europe show similar results despite their differences: Northern Europe has better coverage of sampling stations, and its annual truth fossil CO_2 emissions are lower (an average of 0.20 TgC day^{-1} against 0.59 TgC day^{-1}). In both regions, the posterior fossil CO_2 of the two experiments is far from the truth (Figures 5c and 5e). The posterior biosphere of both regions and experiments is close to each other, with Northern Europe showing a better fit to the truth than Southern Europe, in which the posterior shows a more pronounced positive bias along the year (Figures 6c and 6e).

https://doi.org/10.5194/egusphere-2023-2215
Preprint. Discussion started: 17 October 2023

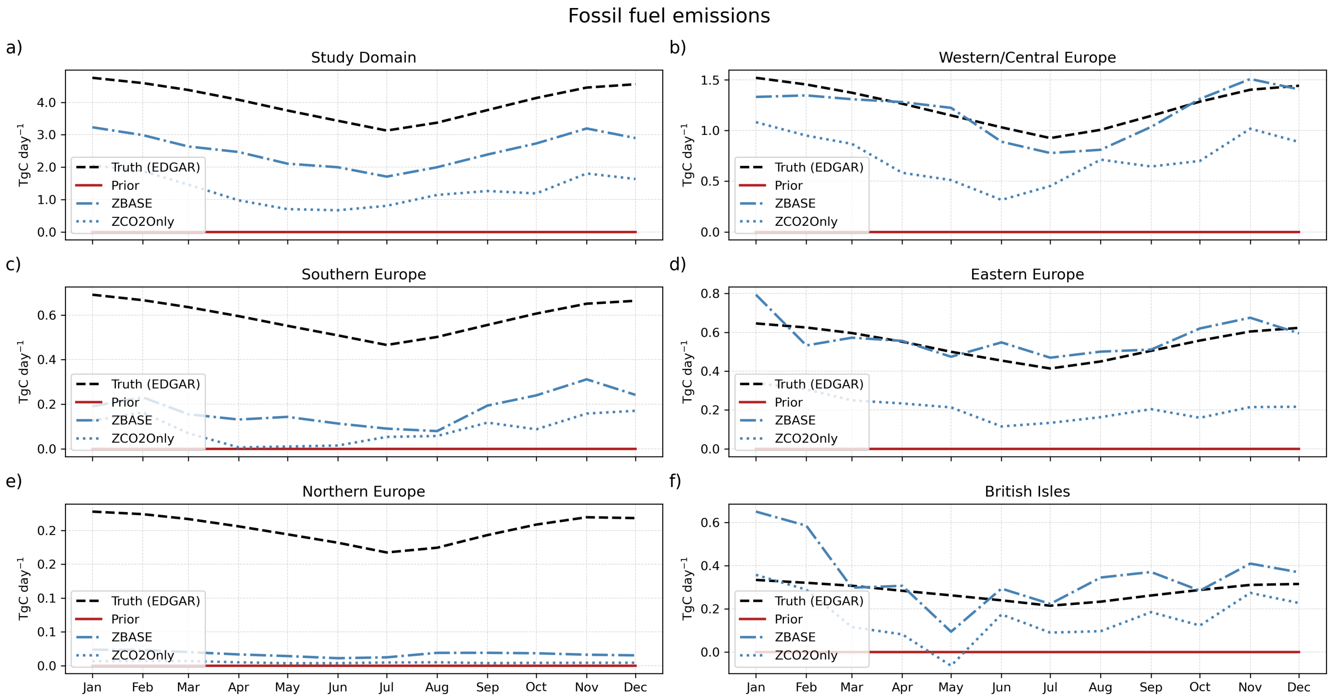

Figure 5. Monthly fossil CO_2 truth (dashed lines), prior (solid lines), and posterior fluxes from the ZBASE (dashed-dotted lines) and ZCO2Only (dotted lines) experiments for a) the study domain and the 5 sub-regions defined: b) Western/Central Europe, c) Southern Europe, d) Eastern Europe, e) Northern Europe, and f) British Isles.

4.2.2 Analysis of the spatial error reduction

We set up the ZBASE and ZCO2Only experiments with prior uncertainties and error structures as in Table 2 based on the values of ODIAC for F_{ff} and VPRM for F_{bio}. Therefore, the model had some information about the spatial and temporal error structure of the prior fluxes. To evaluate the spatial performance of LUMIA, we calculate pixel-level annual total prior RMSE of each experiment and flux category (fossil and biosphere) and the relative RMSE reduction comparing the two experiments for each flux category (Figure 7) defined as:

$$RMSE_{\mathrm{reduction}} = ((RMSE^{apos}_{\mathrm{ZCO2Only}} - RMSE^{apos}_{\mathrm{ZBASE}}) - \mu)/\sigma \qquad (9)$$

where μ is the average value of the difference between the two RMSEs and σ its standard deviation. Here, positive values of $RMSE_{\mathrm{reduction}}$ indicate posterior $RMSE^{apos}_{\mathrm{ZBASE}}$ values that are lower than $RMSE^{apos}_{\mathrm{ZCO2Only}}$, i.e. pixels where when adding $\Delta^{14}C$ observations (ZBASE) shows values closer to the truth (better performance, lower RMSE) than when only having CO_2 observations (ZCO2Only). Since the prior here is zero, the prior RMSE maps (Figures 7a and 7c) show the locations where fluxes have their larger values (either negative or positive for biosphere) during the year. For fossil fuel, we find higher values

https://doi.org/10.5194/egusphere-2023-2215
Preprint. Discussion started: 17 October 2023

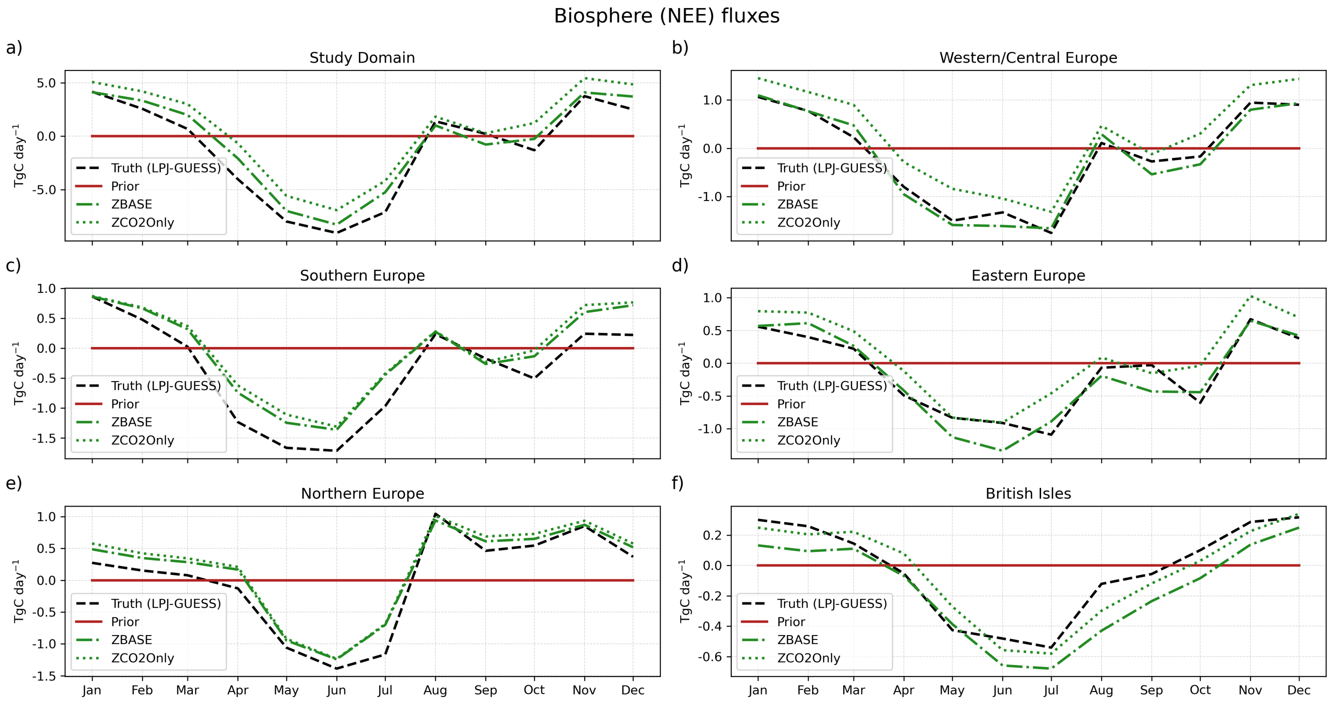

Figure 6. Monthly biosphere (NEE) truth (dashed lines), prior (solid lines), and posterior fluxes from the ZBASE (dashed-dotted lines) and ZCO2Only (dotted lines) experiments for a) the study domain and the 5 sub-regions defined: b) Western/Central Europe, c) Southern Europe, d) Eastern Europe, e) Northern Europe, and f) British Isles.

in Western/Central Europe, but as well some pixels show the location of larger cities like in southern England, Poland, and Spain (Figure 7a). For the biosphere fluxes, we find the stronger RMSE values in Western/Central Europe and the British Isles (Figures 7c).

The largest positive RMSE reductions (where ZBASE performs better than ZCO2Only) (Figures 7b and 7d) occurs around the sampling stations in Western/Central Europe and the British Isles for both flux categories. For fossil CO_2, most of the study domain has positive values (92%), although a large part of these values (around 75%) is close to zero, representing the values in Southern and Northern Europe where there is a low adjustment of the fluxes when adding $\Delta^{14}C$ observations (Figure 7b). For the biosphere fluxes, despite a lower portion of the study domain (40%) showing an improvement in the posterior estimation when adding $\Delta^{14}C$ observations compared with fossil fuel, this presents a clearer pattern in areas such as southeast England, the northern of Western/Central Europe, Denmark, and southern Sweden, as well as some areas in Eastern Europe.

4.2.3 Recovery of the annual budget

Next, we assess how accurately the model can estimate the annual budget for fossil fuel, biosphere (NEE), and the total CO_2. Figure 8 shows the annual budget of the study domain, the sub-regions (right), and some of the largest European countries

https://doi.org/10.5194/egusphere-2023-2215
Preprint. Discussion started: 17 October 2023

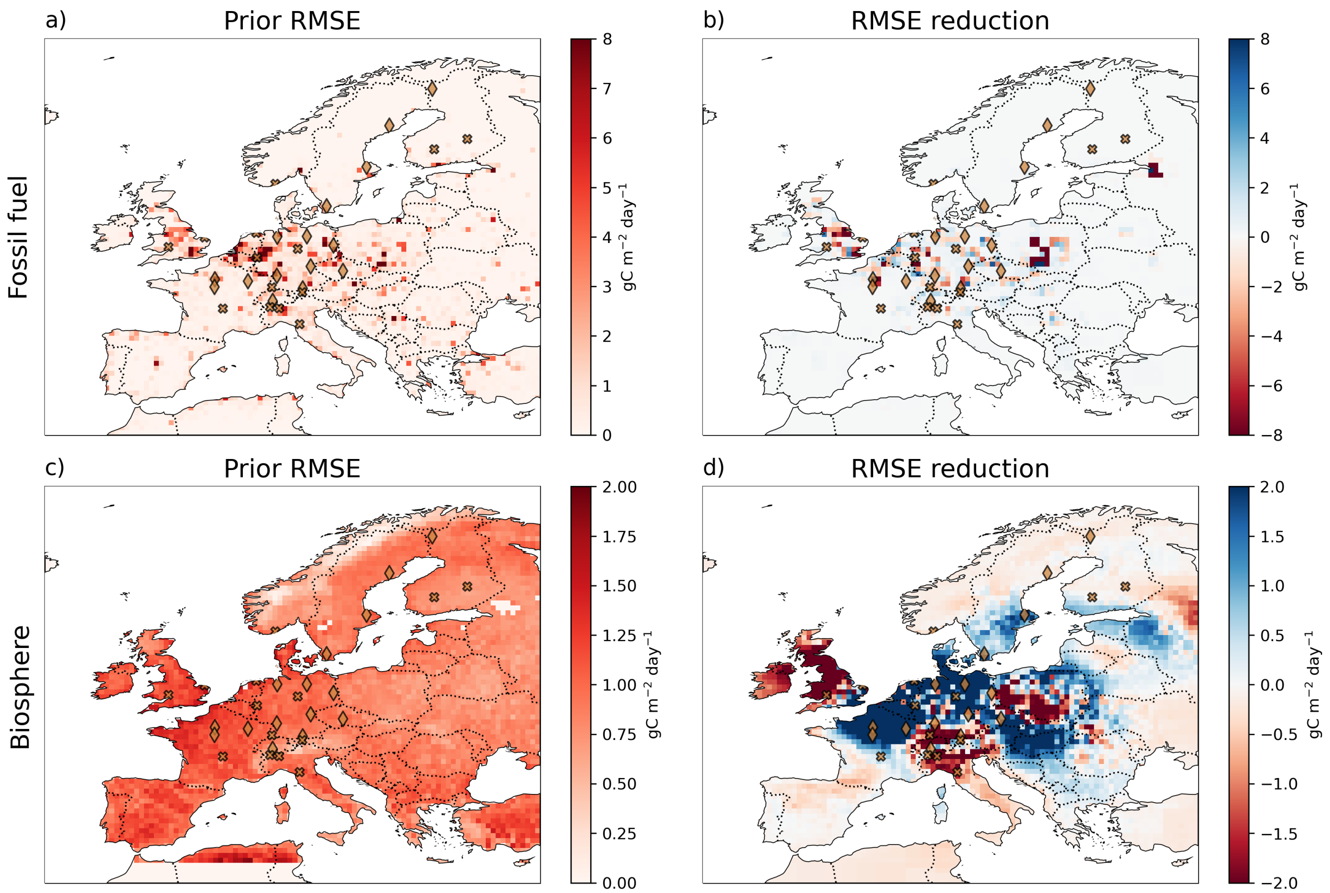

Figure 7. Spatial error of fossil CO_2 (a to d) and biosphere (e to h) for the ZBASE and ZCO2Only experiments. a) and c) show the prior RMSE for F_{ff} and F_{bio}, respectively, and b) and d) show the relative RMSE reduction (see Equation 9) for fossil and biosphere. In Figures b) and d), positive values (in blue) show the pixels where ZBASE performs better than ZCO2Only (i.e. adding Δ^{14}C observations improves the posterior estimates), and negative values (in red) where ZCO2Only performs better than ZBASE. Crosses and diamonds represent stations that only measure CO_2 and those that additionally measure Δ^{14}C, respectively.

by area (left). We include the ODIAC emission inventory and the VPRM product for the biosphere in Figure 8 as references since we base the prior uncertainty and error structure on the spatial and temporal distribution of these two products. As we find in the temporal distribution (Figure 5), in the study domain, the posterior fossil CO_2 from both experiments does not fit the truth, but ZBASE shows a lower bias from the truth than ZCO2Only. This result is reflected in the annual budget, where ZBASE recovers 63% from $\hat{F}_{\mathrm{ff}}$ while ZCO2Only recovers only 32% (Figure 8a). Likewise, the posterior F_{bio} of ZBASE that closely fits $\hat{F}_{\mathrm{bio}}$, recovers 38% of the biosphere budget (Figure 8b), while ZCO2Only, which shows a larger positive bias in the temporal distribution, returns a positive annual budget, contrary to the negative annual budget of the true biosphere fluxes. This behavior is repeated in most of the regions and countries shown in Figure 8, where ZCO2Only strongly underestimates

https://doi.org/10.5194/egusphere-2023-2215
Preprint. Discussion started: 17 October 2023

the annual fossil CO_2 emissions, with the lowest estimates in Southern (15%) and Northern Europe (2%), the latter with a strong underestimation from ZBASE as well (9%), France (33%), and Spain ($\sim$ 0%), which has a similar situation as Northern Europe (5% recovery for ZBASE), and returns an annual biosphere budget that compensates for the total CO_2 budget which is close to ZBASE in most of the cases.

Western and Eastern Europe show the best posterior F_{ff} ZBASE values, 95% and 105% of the truth, respectively. However, while some countries in these regions with good sampling coverage, such as the Benelux Union, show good recovery of $\hat{F}_{\mathrm{ff}}$ (96%), some others with fewer neighboring sampling stations, such as France and Poland, show results far from the annual fossil CO_2 emissions: 71% and 166%, respectively. Germany, which has the best coverage in the study domain, shows some overestimation (111%). On the other hand, the biosphere annual budget compensates in most cases for the total CO_2 budget, returning values that over and underestimate the truth, where the only regions with closer values are Western/Central Europe (126%) and Eastern Europe (128%) for the ZBASE experiment (Figure 8c). Finally, we find better estimates of the total CO_2 budget in most cases for the ZBASE experiment, with the largest recovery in Western/Central Europe (91%), Eastern Europe (96%), and Northern Europe (89%) (Figure 8e), and in the country level in Germany (99%) and France (94%) (Figure 8f).

4.3 A realistic setup

The most realistic approach we can take to perform OSSEs is to use a realistic set of prior fluxes that differ substantially from the true fluxes used to generate the synthetic observations. In this section, we perform a series of experiments using the prior F_{ff}, F_{bio}, and F_{biodis} fluxes described in Section 3.1 to evaluate the impact of prescribing different prior fossil CO_2 uncertainty values as well as the impact of the prior F_{biodis} flux product (RndBASU) in the optimization of F_{ff}.

4.3.1 Impact of the prior fossil CO_2 uncertainty

Figure 9 shows the weekly F_{ff} time series for the three experiments using different prior uncertainties (BASE0.1, BASE, and BASE0.3). The EDGAR ($\hat{F}_{\mathrm{ff}}$) and ODIAC (prior) products have different temporal distributions along the year, with ODIAC being flatter than EDGAR, but both with a minimum during summer, for EDGAR in July (3.13 TgC day^{-1}), and for ODIAC in August (3.05 TgC day^{-1}). In the study domain (Figure 9a), the posterior F_{ff} for the three experiments is very close to each other and approaches the truth from January to February and later from August to December. From May to August, there is an increment in the posterior fluxes that depart from $\hat{F}_{\mathrm{ff}}$, and that we find in Western/Central Europe (Figure 9b) and to a greater extent in Eastern Europe, particularly for BASE0.3 (Figure 9d). All three experiments have the same RMSE with respect to the truth, 0.48 TgC day^{-1}, which is lower than the prior RMSE of 0.65 TgC day^{-1}. The posterior F_{ff} time series in Western/Central Europe shows the best results, with the estimates being close to truth, except for June and July. The three experiments show the same performance, reducing the RMSE by 50% (RMSE$_{\mathrm{prior}}$ = 0.26 TgC day^{-1}, RMSE$_{\mathrm{BASE0.1}}$ = 0.13 TgC day^{-1}), but BASE and BASE0.3 show the values farther from the truth in June and July. Northern Europe (Figure 9c), on the other hand, shows priors that are already very close to the truth, with a posterior RMSE equal to the truth of 0.07 TgC day^{-1}. Finally, in Eastern Europe, with the lowest sampling coverage, the three posterior time series degrade the prior estimate.

https://doi.org/10.5194/egusphere-2023-2215
Preprint. Discussion started: 17 October 2023

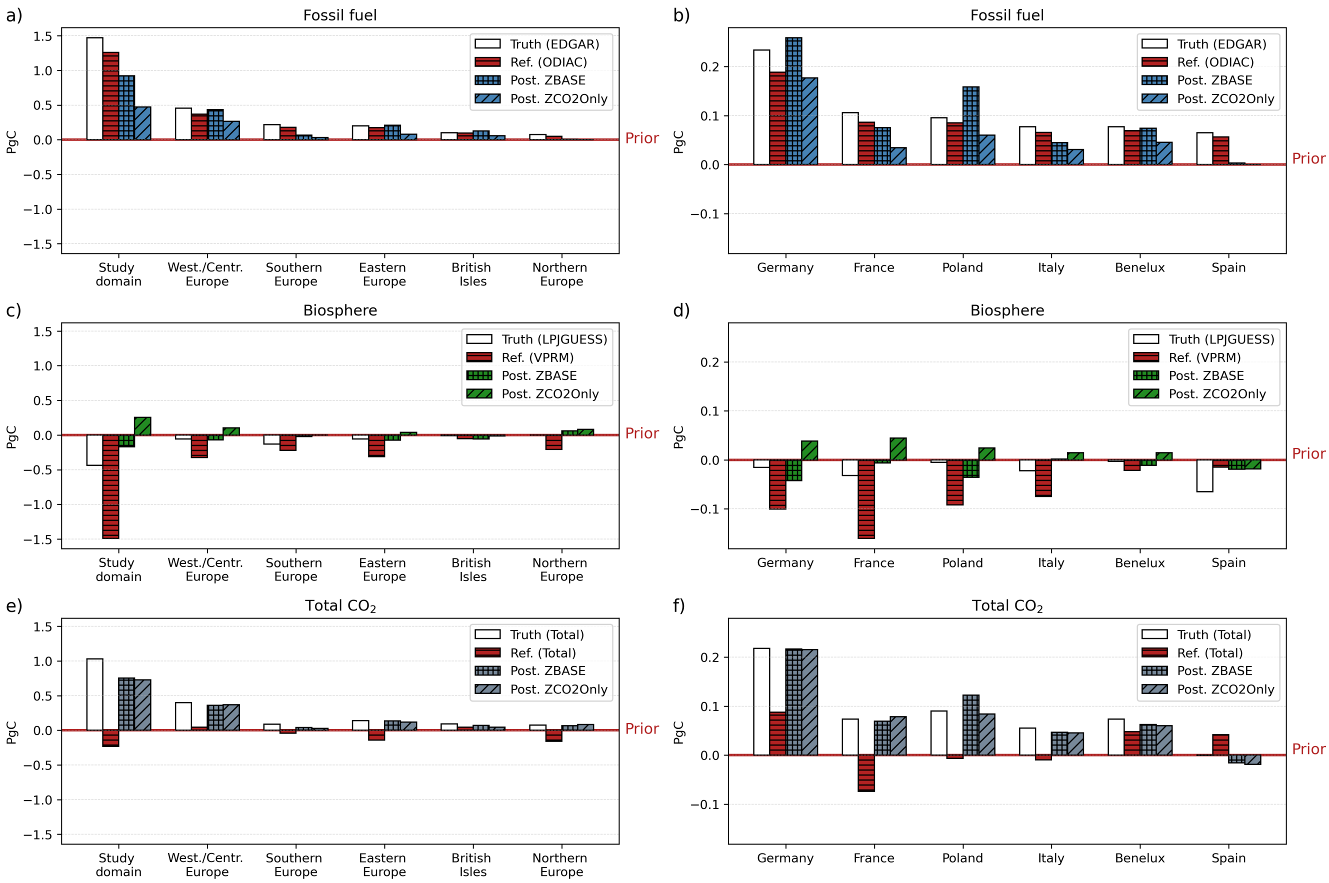

Figure 8. Annual for the study domain, sub-regions (right), and some of the largest European countries by area (left). The white bars show the true emissions based on the EDGAR emission inventory. The red bars (horizontal hatching) are for reference and represent fluxes according to the ODIAC for fossil CO_2 (a and b), VPRM for biosphere (c and d), and the sum of the two for total CO_2 (e and f). The blue, green, and gray bars show the posterior fossil fuel, biosphere, and total CO_2 fluxes for the ZBASE (grid hatching) and ZCO2Only (diagonal hatching) experiments. The red line represents the prior value, 0 PgC.

The difference in the annual budget of EDGAR and ODIAC for the study domain is 0.21 PgC for the year 2018, which is as large as the emission of the country with the largest emission in the study domain for the same year, Germany, with 0.23 PgC according to EDGAR, and 0.19 PgC according to ODIAC. This difference in the study domain is nearly recovered by all three experiments, with BASE0.3 having the highest recovery, 92%. In Western/Central Europe, the three experiments recover 96% of the truth, similar to Germany, where the recovery ranges from 94% for BASE0.1 to 97% for BASE0.3. As we find in the time series (Figure 9d), the prior annual budget is very close to the truth both in Eastern Europe, where the difference is 0.02 PgC, and in Poland, 0.01 PgC. In both cases, the posterior recovers the annual budget, with overestimations from BASE0.3 for

https://doi.org/10.5194/egusphere-2023-2215
Preprint. Discussion started: 17 October 2023

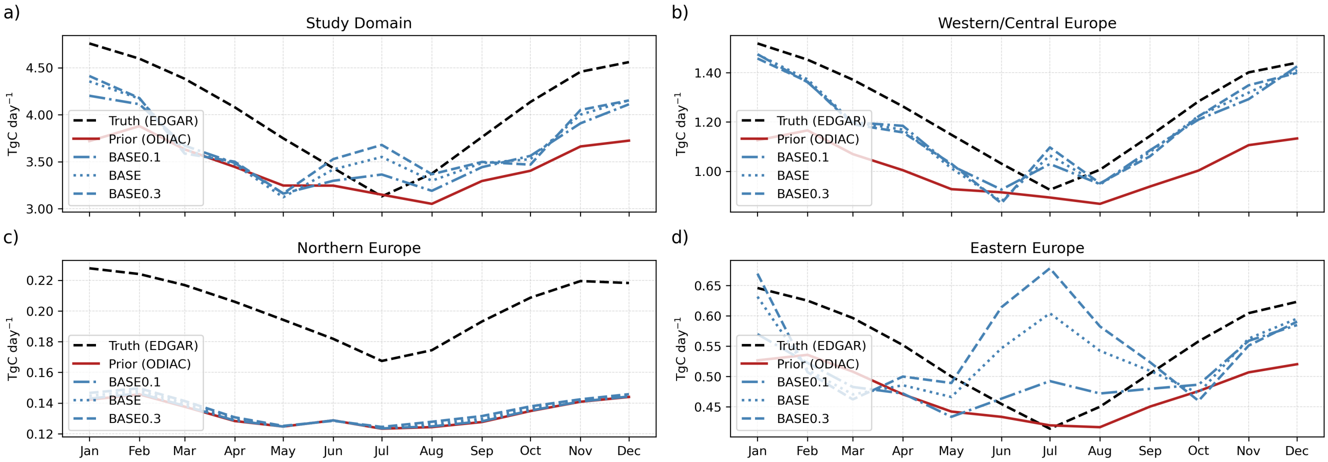

Figure 9. Monthly fossil CO_2 truth (black dashed lines), prior (red solid lines), and posterior fluxes from the BASE0.1 (blue dashed-dotted lines), BASE0.21 (blue dotted lines), and BASE0.3 (blue dashed lines) experiments for a) the study domain and the 3 sub-regions: b) Western/Central Europe, c) Northern Europe, and d) Eastern Europe (note the different scales on the y-axis).

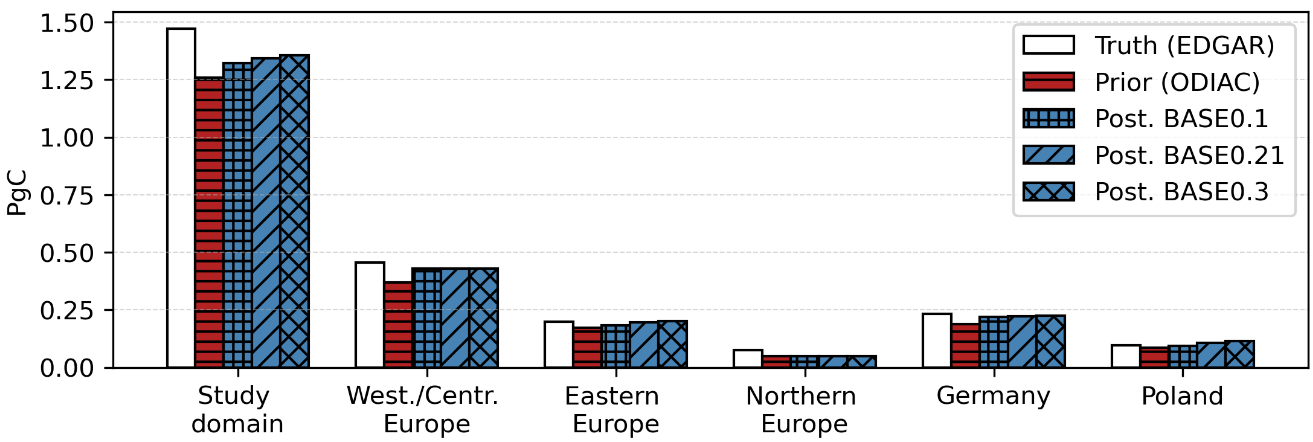

Figure 10. Total annual fossil CO_2 emissions for the study domain, Western/Central Europe, Eastern Europe, Northern Europe, Germany, and Poland. The white bars show the true emissions based on the EDGAR emission inventory. The red bars show the prior fluxes based on the ODIAC emissions inventory. The blue bars show the posterior fossil CO_2 emissions for the BASE0.1 (grid hatching), BASE0.21 (diagonal hatching), and BASE0.3 (cross hatching) experiments.

the whole region and from BASE and BASE0.3 in Poland, which are as big as 120%. Finally, and as expected from Figure 9c, there is no recovery of the annual budget in Northern Europe further than the prior estimate.

https://doi.org/10.5194/egusphere-2023-2215
Preprint. Discussion started: 17 October 2023

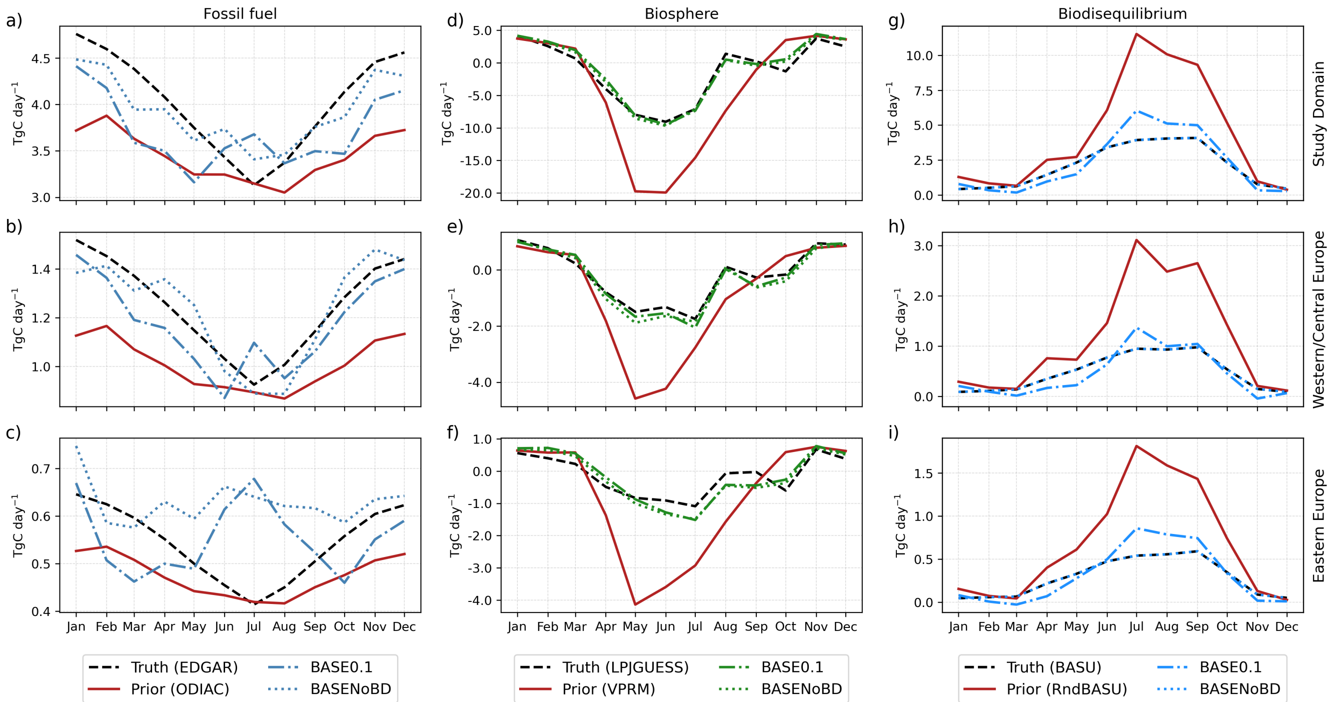

Figure 11. Monthly time series of F_{ff} (a) to c)), F_{bio} (d) to f)), and F_{biodis} (g) to i)), for the study domain (top panel), Western/Central Europe (center panel), and Eastern Europe (bottom panel). The truth is represented in black dashed lines, prior in red solid lines, and posterior fluxes from the BASE0.1 in blue dashed-dotted lines, and BASENoBD in blue dotted lines.

4.3.2 Impact of the terrestrial isotopic disequilibrium product

The prior F_{bio} and F_{biodis} are very different in magnitude from the true values, with differences as large as 13.4 TgC day^{-1} and 7.6 TgC day^{-1}, respectively, during summer for the whole study domain (Figures 11d and 11g). This gap is well resolved for F_{bio} in the study domain and Western/Central Europe (Figures 11d and 11f), and with some underestimation in Eastern Europe between June and September (Figure 11e). However, for the posterior F_{biodis} we find some larger differences from the truth during June and September in the study domain and the two sub-regions. When we prescribe F_{biodis} (BASENoBD), the posterior F_{ff} values from June to August in the study domain and Western/Central Europe (Figures 11a and 11b) get closer to $\hat{F}_{\mathrm{ff}}$, and after the summer in the study domain. This can also be seen in an improvement in the RMSE values with 0.32 TgC day^{-1} for the study domain and 0.10 TgC day^{-1} for Western/Central Europe. In Eastern Europe, the posterior F_{ff} for BASENoBD experiments does not show a significant improvement and, on the contrary, further degrades the prior estimate during the summer and the autumn.

https://doi.org/10.5194/egusphere-2023-2215
Preprint. Discussion started: 17 October 2023

4.3.3 The observational space

Finally, we analyze the model's performance in the observational space, which is crucial for evaluating its effectiveness. Figure 12 compares the prior and posterior concentrations from the BASE0.1 experiment with the corresponding synthetic observations for all sampling stations and, as a representative example, for the Jungfraujoch (JFJ) station. Examining the correlation coefficients, we find that the prior concentrations already correlate significantly with the synthetic observations. The correlation coefficients for the prior estimates are 0.61 for JFJ (Figure 12b) and 0.92 (Figure 12a) for all stations, indicating a reasonable correlation with the synthetic observations. On the other hand, the posterior concentrations exhibit a slight enhancement in the correlation coefficients compared to the prior concentrations: 0.71 for JFJ (Figure 12b) and 0.98 (Figure 12c) for all stations, indicating a refinement in the model's ability to reproduce the synthetic observations accurately. This improvement in correlation coefficients is also reflected in the mismatch plots. For example, the mismatch between the posterior concentrations and the synthetic observations of Δ^{14}C at all stations (Figure 12c) shows a narrower distribution around zero compared to the previous mismatch. This suggests that the inversion process has effectively adjusted the model outputs, bringing them closer to the true observations. Analyzing the concentration time series at the JFJ station (Figure 12e and 12f), we observe that the posterior concentrations agree better with the synthetic observations than the prior concentrations. This improvement is particularly notable for Δ^{14}C, indicating that the inversion has successfully captured the dynamics of this tracer. Lastly, we consider the χ^2 values for the prior and posterior concentrations across all sampling stations and observations. The prior χ^2 value is 1.52, indicating some discrepancy between the prior concentrations and the synthetic observations. However, the posterior χ^2 value improves to 1.00, indicating a closer match between the posterior concentrations and the observed data. These results confirm that the inversion process has effectively improved the model's performance in the observational space.

5 Discussion

Under the current sampling strategy and observation network, we demonstrate through OSSEs that adding $\Delta^{14}CO_2$ observations can help us constrain fossil CO_2 emissions over Europe using the LUMIA system. We start with two simulation experiments in which we set the prior fossil CO_2 and biosphere (Net Ecosystem Exchange, NEE) flux to zero: ZBASE and ZCO2Only. Since flux products (truth and prior) can have similar spatial and temporal distributions in an OSSE setup, it can be easy for the model to retrieve the true values even without adding $\Delta^{14}CO_2$ observations. For this reason, we set up these two experiments in a very challenging way for the model to assess the capabilities of the model to constrain the fossil CO_2 emissions and the biosphere fluxes using CO_2 and $\Delta^{14}CO_2$. The ZBASE and ZCO2Only experiments show us that in regions with a dense sampling network, such as Western/Central Europe, when adding $\Delta^{14}CO_2$ observations, LUMIA is capable of recovering the seasonality of F_{ff} and F_{bio} (Figures 5 and 6), as well as the total annual CO_2 budget (Figure 8) of the whole region and some of the larger countries (also in terms of fossil CO_2 emissions) such as Germany and France. On the other hand, Northern Europe, which has a relatively good network coverage, does not show as good results as Western/Central Europe in the case of fossil CO_2. Comparing the ranges of the true fossil CO_2 and biosphere fluxes in Northern and Western/Central Europe, we find that, while $\hat{F}_{\text{bio}}$ has a similar range in both regions (-2.22 to 1.47 TgC day^{-1} in Northern Europe and -2.26 to

https://doi.org/10.5194/egusphere-2023-2215
Preprint. Discussion started: 17 October 2023

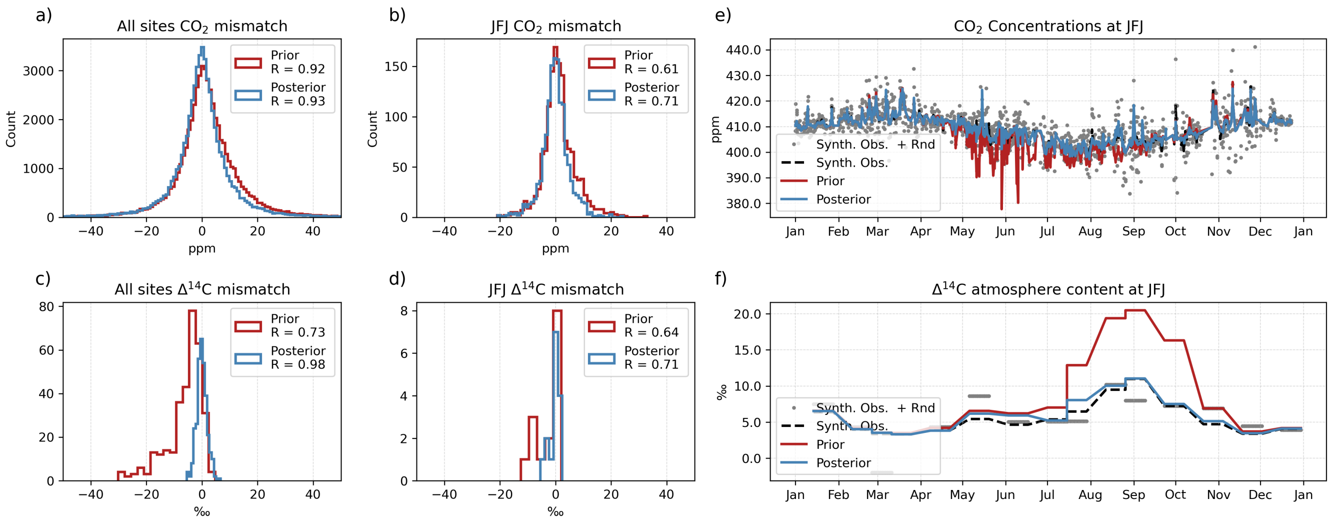

Figure 12. Mismatches between the synthetic observations and the prior (red) and posterior (blue) concentrations for all the sampling stations and at Jungfraujoch ICOS station for CO_2 (a and b) and for $\Delta^{14}C$ (c and d). The right panel shows the time series of CO_2 (e) and $\Delta^{14}C$ (f) at Jungfraujoch. All prior and posterior concentrations correspond to the BASE0.1 experiment.

1.21 TgC day^{-1} in Western/Central Europe), $\hat{F}_{\mathrm{ff}}$ differs by one order of magnitude: 0.16 to 0.23 1.47 TgC day^{-1} in Northern Europe and 0.91 to 1.52 TgC day^{-1} in Western/Central Europe. Using the concept of signal-to-noise ratio, if we consider the fossil CO_2 as the signal (the variable in which we are more interested) and the biosphere as the noise, this difference of one order of magnitude between them in Northern Europe makes it easier for the model to recover the biosphere fluxes than the fossil CO_2 emissions, even with additional information about $\Delta^{14}C$.

This situation is also clear in the study domain and the other regions. The terrestrial biosphere flux (NEE) exhibits a large seasonal pattern that provides a strong enough signal from the inversion to generate this temporal pattern in the posterior F_{bio} for the whole study domain and the sub-regions (Figure 6) for both experiments, despite the bias that we find in most of the regions. However, the fossil CO_2 seasonality is not as strong as the NEE on a regional scale, and with poor sampling coverage and no information about $\Delta^{14}C$, it is impossible for the model to retrieve the seasonality of the fossil CO_2 emissions in regions such as Southern Europe, Eastern Europe, and the British Isles. These results are confirmed by the BASE experiments, in which inversions improve the posterior fossil CO_2 time series (Figure 10) and annual budget (Figures 9d and 11), but not in regions lacking observations, such as Eastern Europe.

Wang et al. (2018) found similar results in Europe despite large differences between their inversion implementation and our LUMIA system. The main differences lie in the transport model and the inversion approach. They use a global transport model at a resolution of $3.75° \times 2.5°$ (Laboratoire de Météorologie Dynamique's LMDZv4) and a precalculated fossil CO_2 tracer (product of the mass balance), while we use a Lagrangian regional transport model at a higher horizontal resolution ($0.5° \times 0.5°$) and optimize both the fossil and the natural fluxes using as tracers CO_2 and $\Delta^{14}CO_2$. Wang et al. (2018) found

https://doi.org/10.5194/egusphere-2023-2215
Preprint. Discussion started: 17 October 2023

the largest error reductions around Germany, Benelux, and eastern France, where most sampling stations are located. Northern Europe was also poorly constrained in their inversions, similar to what we find. Wang et al. (2018) attributed the results in Northern Europe to the coarse spatial resolution of the transport model. But even with a higher resolution transport model as employed in LUMIA, we can still not resolve the true fossil CO_2 emissions in an OSSE setup given the current CO_2 and $\Delta^{14}CO_2$ observation networks. A more likely explanation is the difference in the magnitude of the fossil CO_2 emissions in the region against the natural fluxes and other regions. A workaround can be the normalization of the fluxes or the implementation of regional scaling factors that allow having similar magnitudes across the study domain but still, the impact from other sources of noise, such as the background concentration (boundary condition), which includes the fluxes transported from other regions within the domain, can make it difficult to solve.

The realistic approach shows us that the posterior fossil CO_2 emissions are not very sensitive to the prescribed prior uncertainty in regions with a dense sampling network. This is a positive result since the prior uncertainty is difficult to define both in magnitude and in spatial and temporal structure. Basu et al. (2016), for example, defined the prior uncertainty as the inter-prior spread (i.e. the difference among multiple prior F_{ff} products), and as they pointed out in the study, this inter-prior spread is comparable in magnitude with the annual average NEE estimated by CarbonTracker. Both Basu et al. (2016) and Wang et al. (2018) highlight the importance of a regional horizontal correlation and error structure for fossil CO_2 emissions. In this study, we use the same horizontal correlation and error structures developed by Monteil et al. (2020) originally for NEE. We are aware of the necessity of defining specific structures for fossil CO_2 within LUMIA due to the low improvement in spatial terms that we find in Figure 7 when adding $\Delta^{14}CO_2$ observations. However, it is important to mention that given the sparse observation network, we can expect spatial misattributions (flux corrections that should happen in one place but are instead made elsewhere), and therefore, we should interpret the results aggregated at the scale that is relevant given the model setup, as we demonstrate through the time series and annual budget results.

We also find the prior terrestrial disequilibrium product to have an important impact on the posterior fossil CO_2 emissions (Figure 11). According to Turnbull et al. (2009), one of the main contributors to atmospheric $\Delta^{14}CO_2$ is heterotrophic respiration in natural environments. Therefore, having a good prior F_{biodis} estimate is crucial in estimating posterior F_{ff}. The impact of F_{biodis} and the other $\Delta^{14}CO_2$ flux terms is not negligible and will be explored in a follow-up study. Particularly, the emissions from nuclear facilities can have a larger impact than the terrestrial disequilibrium (Graven and Gruber, 2011). In this study, we fixed the F_{nuc} term, and hence, its impact is not considered here. However, available information about radiocarbon emissions from nuclear facilities is only available annually (Graven and Gruber, 2011; Zazzeri et al., 2018) that are usually distributed constantly throughout the year, while in reality, nuclear facilities have routine gas releases during periodic purges and venting. This variability in nuclear emissions has been only studied by measuring the atmospheric content of $\Delta^{14}CO_2$ in the surrounding areas of single nuclear power plant facilities (Turnbull et al., 2014; Vogel et al., 2013; Lehmuskoski et al., 2021), but not yet in a large regional setup, and therefore it needs further investigation.

https://doi.org/10.5194/egusphere-2023-2215
Preprint. Discussion started: 17 October 2023

6 Conclusions and future perspectives

We have expanded the LUMIA system to be capable of simultaneously inverting atmospheric observations of CO_2 and $\Delta^{14}CO_2$ to estimate fossil CO_2 emissions and net terrestrial biosphere CO_2 fluxes over Europe. We performed the first observing system simulation experiments to test the performance of the $\Delta^{14}C$-enhanced LUMIA version. In the first set of experiments, we show the impact of adding $\Delta^{14}C$ observations in a scenario with prior estimates of F_{ff} and F_{bio} set to zero. In regions with good sampling network coverage, assimilating both CO_2 and $\Delta^{14}C$ observations allows recovering the seasonality of F_{ff} and F_{bio} and the annual F_{ff} budget, while when assimilating only CO_2 observations, the posterior F_{ff} is degraded. In the second set of experiments, we performed OSSES using more realistic priors to test the impact of the prescribed F_{ff} uncertainty and the impact of the prior F_{biodis} product. The prescribed prior uncertainty has no significant impact on the posterior F_{ff}. On the other hand, the prior F_{biodis} product can significantly impact the posterior F_{ff}.

In future work, we will revisit the impact of the prior F_{biodis} product using simulated terrestrial biosphere disequilibrium estimates by the LPJ model following the methodology by Scholze et al. (2003). We will also evaluate the impact of the prior F_{nuc}, the sampling strategy, and the network density of the $\Delta^{14}C$ observations on the capability to estimate fossil CO_2 emissions. The current 2-weekly integrated sampling strategy allows us to get a reasonable estimate of the annual budget over the whole domain. But the inversion can neither recover the correct temporal behavior nor the spatial distribution of the fossil CO_2 emission when using $C\Delta^{14}C$ observations provided by the current 2-weekly integrated sampling strategy. Additionally, converting $\Delta^{14}C$ values to $C\Delta^{14}C$ implies calculating the average of the CO_2 observations during the 2-week integration period that can introduce additional errors that we did not account for in this study. We will evaluate the use of hourly flask samples under different strategies as described by Levin et al. (2020), such as a "smart" sampling based on pollution episodes of CO_2 and CO. This will be in preparation for the intensive $\Delta^{14}C$ sampling campaign (hourly samples taken every third day) planned within the EC's Horizon Europe CORSO (CO2MVS Research on Supplementary Observations) project (https://corso-project.eu/) during 2024 at 10 ICOS stations located in Western Europe.

Code availability. The LUMIA source code used in this paper has been published on Zenodo and can be accessed at https://doi.org/10.5281/zenodo.8426217.

Data availability. The revised EDGARv4.3 https://doi.org/10.18160/GFNT-5Y47, LPJ-GUESS https://doi.org/10.18160/p52c-1qjm, and VPRM https://doi.org/10.18160/VX78-HVA1 datasets are availabale from the ICOS-Carbon Portal. ODIAC data is available at https://doi.org/10.17595/20170411.001. The input data has been uploaded on Figshare and is available at https://doi.org/10.6084/m9.figshare.24307162.

https://doi.org/10.5194/egusphere-2023-2215
Preprint. Discussion started: 17 October 2023

Appendix A: Summary of ocean and ocean disequilibrium-derived synthetic observations

Table A1.

Station	Ocean CO_2 ppm	Ocean $\Delta^{14}C$ ‰	Ocedis $\Delta^{14}C$ ‰	Synth. Obs. CO_2 ppm	Synth. Obs. (rnd) CO_2 ppm	Obs. Error CO_2 ppm	Synth. Obs. $\Delta^{14}C$ ‰	Synth. Obs. (rnd) $\Delta^{14}C$ ‰	Obs. Error $\Delta^{14}C$ ‰
All sites	-0.07 ± 0.15	-0.007 ± 0.007	0.02 ± 0.017	414.6 ± 12.7	414.6 ± 18.3	9.8 ± 9.0	0.3 ± 8.0	0.2 ± 8.4	1.9 ± 0.05
GAT	-0.07 ± 0.1	-0.008 ± 0.007	0.021 ± 0.014	415.7 ± 12.7	416.2 ± 19.2	11.1 ± 7.2	2.1 ± 4.2	2.6 ± 4.8	1.9 ± 0.05
HPB	-0.04 ± 0.05	-0.005 ± 0.003	0.016 ± 0.008	414.0 ± 11.2	414.5 ± 16.7	10.4 ± 6.3	1.0 ± 6.3	1.5 ± 6.8	1.9 ± 0.04
HTM	-0.07 ± 0.12	-0.009 ± 0.009	0.016 ± 0.009	415.4 ± 12.3	415.5 ± 16.8	10.0 ± 5.7	1.0 ± 4.5	0.5 ± 4.8	1.9 ± 0.04
JFJ	-0.03 ± 0.04	-0.002 ± 0.002	0.01 ± 0.005	409.1 ± 5.0	409.0 ± 6.9	4.2 ± 2.1	5.5 ± 2.3	5.5 ± 2.9	2.0 ± 0.02
KIT	-0.06 ± 0.06	-0.005 ± 0.004	0.024 ± 0.012	427.1 ± 16.9	427.4 ± 26.9	17.7 ± 10.0	-5.2 ± 10.5	-4.7 ± 11.0	1.9 ± 0.05
KRE	-0.05 ± 0.06	-0.005 ± 0.004	0.014 ± 0.009	415.3 ± 12.6	415.0 ± 16.9	10.3 ± 6.0	-4.0 ± 4.6	-4.2 ± 4.9	1.9 ± 0.05
LIN	-0.06 ± 0.09	-0.007 ± 0.006	0.017 ± 0.011	420.9 ± 16.9	420.2 ± 25.2	15.2 ± 11.6	-7.7 ± 9.4	-8.2 ± 9.5	1.9 ± 0.05
NOR	-0.07 ± 0.14	-0.009 ± 0.009	0.011 ± 0.01	415.8 ± 10.7	415.5 ± 14.4	8.5 ± 4.8	4.9 ± 4.3	4.5 ± 5.1	1.9 ± 0.03
OPE	-0.07 ± 0.08	-0.006 ± 0.004	0.034 ± 0.021	416.7 ± 14.3	416.5 ± 21.5	13.3 ± 9.3	-1.6 ± 6.8	-1.2 ± 6.3	1.9 ± 0.04
OXK	-0.06 ± 0.08	-0.006 ± 0.004	0.02 ± 0.013	411.0 ± 7.3	410.8 ± 10.5	7.1 ± 3.0	1.8 ± 4.8	1.5 ± 5.8	1.9 ± 0.03
PAL	-0.1 ± 0.13	-0.011 ± 0.007	0.005 ± 0.004	412.3 ± 8.6	412.3 ± 10.8	6.0 ± 3.7	8.7 ± 4.2	8.9 ± 5.0	1.9 ± 0.03
SAC	-0.08 ± 0.1	-0.009 ± 0.007	0.04 ± 0.02	425.2 ± 23.0	425.6 ± 37.9	23.1 ± 20.0	-13.1 ± 8.3	-13.7 ± 8.8	1.9 ± 0.03
STE	-0.08 ± 0.12	-0.01 ± 0.007	0.021 ± 0.01	413.4 ± 10.0	413.7 ± 15.6	9.4 ± 7.2	0.4 ± 4.9	-0.4 ± 6.2	1.9 ± 0.03
SVB	-0.1 ± 0.16	-0.011 ± 0.009	0.007 ± 0.006	412.5 ± 9.5	412.0 ± 12.4	7.1 ± 4.5	5.8 ± 3.0	5.5 ± 3.7	1.9 ± 0.03
TRN	-0.08 ± 0.09	-0.009 ± 0.007	0.041 ± 0.026	415.9 ± 13.7	415.7 ± 21.0	12.2 ± 10.7	2.8 ± 5.4	3.1 ± 6.1	1.9 ± 0.04
BIR	-0.09 ± 0.1	-	-	410.7 ± 7.6	410.6 ± 10.3	6.1 ± 4.1	-	-	-
CMN	-0.03 ± 0.05	-	-	408.4 ± 6.7	408.2 ± 8.8	5.1 ± 2.6	-	-	-
HEL	-0.15 ± 0.25	-	-	414.1 ± 9.3	414.2 ± 16.7	11.1 ± 6.9	-	-	-
IPR	-0.04 ± 0.05	-	-	428.8 ± 17.6	428.8 ± 26.0	16.8 ± 10.3	-	-	-
JUE	-0.07 ± 0.08	-	-	417.6 ± 15.3	416.9 ± 24.8	15.2 ± 15.5	-	-	-
LMP	-0.01 ± 0.27	-	-	410.5 ± 4.6	410.3 ± 6.5	4.5 ± 1.8	-	-	-
LUT	-0.1 ± 0.14	-	-	416.8 ± 15.7	416.8 ± 24.9	14.4 ± 12.7	-	-	-
PRS	-0.02 ± 0.04	-	-	408.9 ± 5.0	409.0 ± 6.7	4.0 ± 2.0	-	-	-
PUI	-0.07 ± 0.12	-	-	410.9 ± 6.1	411.0 ± 8.1	5.1 ± 2.2	-	-	-
PUY	-0.06 ± 0.08	-	-	409.4 ± 8.3	409.3 ± 11.5	6.5 ± 4.2	-	-	-
RGL	-0.11 ± 0.13	-	-	409.6 ± 8.3	409.6 ± 11.1	6.9 ± 3.9	-	-	-
SMR	-0.07 ± 0.13	-	-	414.2 ± 10.6	414.2 ± 13.9	7.9 ± 4.6	-	-	-
SSL	-0.06 ± 0.06	-	-	410.2 ± 6.6	410.4 ± 9.7	6.4 ± 3.1	-	-	-
TOH	-0.06 ± 0.09	-	-	414.7 ± 11.7	414.9 ± 16.4	9.8 ± 5.6	-	-	-
UTO	-0.24 ± 0.45	-	-	414.2 ± 9.2	414.3 ± 14.5	9.4 ± 5.0	-	-	-
WAO	-0.06 ± 0.07	-	-	419.5 ± 9.6	420.2 ± 19.5	14.0 ± 7.5	-	-	-
WES	-0.08 ± 0.12	-	-	414.1 ± 10.3	414.2 ± 18.6	13.0 ± 6.9	-	-	-
ZSF	-0.03 ± 0.04	-	-	409.1 ± 5.3	409.2 ± 7.4	4.7 ± 2.3	-	-	-

https://doi.org/10.5194/egusphere-2023-2215
Preprint. Discussion started: 17 October 2023

Appendix B: Spatial clustering algorithm

The inversion solves for offsets to the prior fluxes at a variable spatial resolution: high (up to 0.25°) in the direct vicinity of observation sites, but lower in parts of the domain that are not well sampled by the observation network. To achieve this, the spatial domain of the inversion is divided into a set of clusters of grid cells, each defined by the following properties:

- cells: the list of grid cells included in the cluster.
- weight: the sum of a property carried by each grid cell. In our case, this property is the average sensitivity of the observation network to that grid cell.
- size: the number of grid cells in the cluster.
- mean_lat, mean_lon: the average (area-weighted) lat and lon of the grid cells in the cluster
- area: the total of all the grid cells included in the cluster.
- type: ocean, land, or mixed.
- continuity: whether it is possible to "walk" from any grid cell of the cluster to any other one or whether there are discontinuities (e.g. a "land" cluster separated in two parts by ocean grid cells).

The objective of the clustering algorithm is to divide the domain into a user-defined number of continuous clusters with roughly equal "weight". The "weight" of a single grid cell is, in our case, defined as the average value of the adjoint field in that grid cell for an adjoint simulation driven by model-data mismatches set proportional to the uncertainty of each observation. The clustering is performed iteratively as follows:

1. Initially, one single cluster is formed, comprising all grid cells of the domain. It is added to a pool of "dividable" clusters.
2. The "weight" of all clusters in that pool is calculated (i.e. the weight of the single initial cluster at the first iteration);
3. The cluster with the largest weight is then split into two even parts across its longest axis (i.e., in an eastern and western part, at the first iteration);
4. The resulting two new clusters are checked for continuity. If needed, they are further split into several continuous clusters;
5. If a cluster reaches the minimum size (1 grid cell), it is moved to a pool of "defined" clusters.
6. If the total number of clusters ("dividable" plus "defined") is lower than the target number of clusters, then repeat steps 2 to 6. Otherwise, exit.

Because of how the cluster weights are defined, clusters away from observation points end up being considerably larger, but they are in regions where the inversions would have applied very smooth flux adjustments, so there is no real drawback to this clustering.

https://doi.org/10.5194/egusphere-2023-2215
Preprint. Discussion started: 17 October 2023

Author contributions. All authors designed the experiments, CG and GM developed the code, SB provided the $\Delta^{14}CO_2$ data, and CG performed the simulations. CG prepared the paper, and GM, SB, and MS provided corrections and suggestions for improvements.

Competing interests. The authors declare that they have no conflict of interest.

Acknowledgements. We thank the Swedish Research Council for Sustainable Development FORMAS for funding the 14C-FFDAS project (Dnr 2018-01771). MS, GM, and CG acknowledge support from the EU projects AVENGERS (Grant Agreement (GA): 101081322) and CORSO (GA: 101082194) as well as from the three Swedish strategic research areas ModElling the Regional and Global earth system (MERGE), the e-science collaboration (eSSENCE), and Biodiversity and Ecosystems in a Changing Climate (BECC). SB acknowledges the National Aeronautics and Space Administration NASA grant 80NSSC21K1708 and NASA/ESSIC cooperative agreement 80NSSC23M0011. The computations were enabled by resources provided by the National Academic Infrastructure for Supercomputing in Sweden (NAISS), the Swedish National Infrastructure for Computing (SNIC) at LUNARC, and NSC partially funded by the Swedish Research Council through grant agreements no. 2022-06725 and no. 2018-05973, and the Royal Physiographic Society of Lund through Endowments for the Natural Sciences, Medicine and Technology - Geoscience.

https://doi.org/10.5194/egusphere-2023-2215
Preprint. Discussion started: 17 October 2023

References

Basu, S., Guerlet, S., Butz, A., Houweling, S., Hasekamp, O., Aben, I., Krummel, P., Steele, P., Langenfelds, R., Torn, M., Biraud, S., Stephens, B., Andrews, A., and Worthy, D.: Global CO2 fluxes estimated from GOSAT retrievals of total column CO2, Atmos. Chem. Phys., 13, 8695–8717, https://doi.org/10.5194/acp-13-8695-2013, 2013.

Basu, S., Miller, J. B., and Lehman, S.: Separation of biospheric and fossil fuel fluxes of CO2 by }atmospheric inversion of CO2 and 14CO2 measurements: Observation System Simulations, Atmos. Chem. Phys., 16, 5665–5683, https://doi.org/10.5194/acp-16-5665-2016, 2016.

Basu, S., Lehman, S. J., Miller, J. B., Andrews, A. E., Sweeney, C., Gurney, K. R., Xu, X., Southon, J., and Tans, P. P.: Estimating US fossil fuel CO2 emissions from measurements of 14C in atmospheric CO2, Proceedings of the National Academy of Sciences, 117, 13 300–13 307, https://doi.org/10.1073/pnas.1919032117, 2020.

Bocquet, M., Elbern, H., Eskes, H., Hirtl, M., Žabkar, R., Carmichael, G. R., Flemming, J., Inness, A., Pagowski, M., Pérez Camaño, J. L., Saide, P. E., San Jose, R., Sofiev, M., Vira, J., Baklanov, A., Carnevale, C., Grell, G., and Seigneur, C.: Data assimilation in atmospheric chemistry models: current status and future prospects for coupled chemistry meteorology models, Atmos. Chem. Phys., 15, 5325–5358, https://doi.org/10.5194/acp-15-5325-2015, 2015.

Bréon, F. M., Broquet, G., Puygrenier, V., Chevallier, F., Xueref-Remy, I., Ramonet, M., Dieudonné, E., Lopez, M., Schmidt, M., Perrussel, O., and Ciais, P.: An attempt at estimating Paris area CO2 emissions from atmospheric concentration measurements, Atmos. Chem. Phys., 15, 1707–1724, https://doi.org/10.5194/acp-15-1707-2015, 2015.

Brioude, J., Angevine, W. M., Ahmadov, R., Kim, S.-W., Evan, S., McKeen, S. A., Hsie, E.-Y., Frost, G. J., Neuman, J. A., Pollack, I. B., Peischl, J., Ryerson, T. B., Holloway, J., Brown, S. S., Nowak, J. B., Roberts, J. M., Wofsy, S. C., Santoni, G. W., Oda, T., and Trainer, M.: Top-down estimate of surface flux in the Los Angeles Basin using a mesoscale inverse modeling technique: assessing anthropogenic emissions of CO, NO_x and CO₂ and their impacts, Atmos. Chem. Phys., 13, 3661–3677, https://doi.org/10.5194/acp-13-3661-2013, 2013.

Chatterjee, A. and Michalak, A. M.: Technical Note: Comparison of ensemble Kalman filter and variational approaches for CO₂ data assimilation, Atmos. Chem. Phys., 13, 11 643–11 660, https://doi.org/10.5194/acp-13-11643-2013, 2013.

Chevallier, F., Bréon, F.-M., and Rayner, P. J.: Contribution of the Orbiting Carbon Observatory to the estimation of CO2 sources and sinks: Theoretical study in a variational data assimilation framework, Journal of Geophysical Research: Atmospheres, 112, https://doi.org/https://doi.org/10.1029/2006JD007375, 2007.

Eyring, V., Gillett, N. P., Achuta Rao, K. M., Barimalala, R., Barreiro Parrillo, M., Bellouin, N., Cassou, C., Durack, P. J., Kosaka, Y., McGregor, S., Min, S., Morgenstern, O., and Sun, Y.: Human Influence on the Climate System, in: Climate Change 2021: The Physical Science Basis. Contribution of Working Group I to the Sixth Assessment Report of the Intergovernmental Panel on Climate Change, edited by Masson-Delmotte, V., Zhai, P., Pirani, A., Connors, S. L., Péan, C., Berger, S., Caud, N., Chen, Y., Goldfarb, L., Gomis, M. I., Huang, M., Leitzell, K., Lonnoy, E., Matthews, J. B. R., Maycock, T. K., Waterfield, T., Yelekçi, O., Yu, R., and Zhou, B., p. 423–552, Cambridge University Press, Cambridge, United Kingdom and New York, NY, USA, https://doi.org/10.1017/9781009157896.005, 2021.

Gerbig, C. and Koch, F.-T.: Biosphere-atmosphere exchange fluxes for CO2 from the Vegetation Photosynthesis and Respiration Model VPRM for 2006-2022, https://doi.org/10.18160/VX78-HVA1, 2021a.

Gerbig, C. and Koch, F.-T.: European anthropogenic CO2 emissions based on EDGARv4.3, BP statistics 2021 and CarbonMonitor for 2019-2020 (Version 1.0). ICOS ERIC – Carbon Portal, https://doi.org/https://doi.org/10.18160/GFNT-5Y47, 2021b.

Graven, H., Keeling, R. F., and Rogelj, J.: Changes to Carbon Isotopes in Atmospheric CO2 Over the Industrial Era and Into the Future, Global Biogeochemical Cycles, 34, e2019GB006 170, https://doi.org/https://doi.org/10.1029/2019GB006170, 2020.

Graven, H. D. and Gruber, N.: Continental-scale enrichment of atmospheric 14CO2 from the nuclear power industry: potential impact on the estimation of fossil fuel-derived CO2, Atmos. Chem. Phys., 11, 12 339–12 349, https://doi.org/10.5194/acp-11-12339-2011, 2011.

Hahn, V., Högberg, P., and Buchmann, N.: 14C – a tool for separation of autotrophic and heterotrophic soil respiration, Global Change Biology, 12, 972–982, https://doi.org/https://doi.org/10.1111/j.1365-2486.2006.001143.x, 2006.

Han, P., Zeng, N., Oda, T., Lin, X., Crippa, M., Guan, D., Janssens-Maenhout, G., Ma, X., Liu, Z., Shan, Y., Tao, S., Wang, H., Wang, R., Wu, L., Yun, X., Zhang, Q., Zhao, F., and Zheng, B.: Evaluating China's fossil-fuel CO2 emissions from a comprehensive dataset of nine inventories, Atmos. Chem. Phys., 20, 11 371–11 385, https://doi.org/10.5194/acp-20-11371-2020, 2020.

Hesshaimer, V. and Levin, I.: Revision of the stratospheric bomb 14CO2 inventory, Journal of Geophysical Research: Atmospheres, 105, 11 641–11 658, https://doi.org/https://doi.org/10.1029/1999JD901134, 2000.

Hesshaimer, V., Heimann, M., and Levin, I.: Radiocarbon evidence for a smaller oceanic carbon dioxide sink than previously believed, Nature, 370, 201–203, https://doi.org/10.1038/370201a0, 1994.

Hoffman, R. N. and Atlas, R.: Future Observing System Simulation Experiments, Bulletin of the American Meteorological Society, 97, 1601–1616, https://doi.org/10.1175/BAMS-D-15-00200.1, 2016.

Janssens-Maenhout, G., Crippa, M., Guizzardi, D., Muntean, M., Schaaf, E., Dentener, F., Bergamaschi, P., Pagliari, V., Olivier, J. G. J., Peters, J. A. H. W., van Aardenne, J. A., Monni, S., Doering, U., Petrescu, A. M. R., Solazzo, E., and Oreggioni, G. D.: EDGAR v4.3.2 Global Atlas of the three major greenhouse gas emissions for the period 1970–2012, Earth Syst. Sci. Data, 11, 959–1002, https://doi.org/10.5194/essd-11-959-2019, 2019.

Kaminski, T., Scholze, M., Rayner, P., Voßbeck, M., Buchwitz, M., Reuter, M., Knorr, W., Chen, H., Agustí-Panareda, A., Löscher, A., and Meijer, Y.: Assimilation of atmospheric CO2 observations from space can support national CO2 emission inventories, Environmental Research Letters, 17, 014 015, https://doi.org/10.1088/1748-9326/ac3cea, 2022.

Kuc, T., Rozanski, K., Zimnoch, M., Necki, J. M., and Korus, A.: Anthropogenic emissions of CO2 and CH4 in an urban environment, Applied Energy, 75, 193–203, https://doi.org/https://doi.org/10.1016/S0306-2619(03)00032-1, 2003.

Kuhlmann, G., Henne, S., Meijer, Y., and Brunner, D.: Quantifying CO2 Emissions of Power Plants With CO2 and NO2 Imaging Satellites, Frontiers in Remote Sensing, 2, https://www.frontiersin.org/articles/10.3389/frsen.2021.689838, 2021.

Lehman, S. J., Miller, J. B., Wolak, C., Southon, J., Tans, P. P., Montzka, S. A., Sweeney, C., Andrews, A., LaFranchi, B., Guilderson, T. P., and Turnbull, J. C.: Allocation of Terrestrial Carbon Sources Using 14CO2: Methods, Measurement, and Modeling, Radiocarbon, 55, 1484–1495, https://doi.org/DOI: 10.1017/S0033822200048414, 2013.

Lehmuskoski, J., Vasama, H., Hämäläinen, J., Hokkinen, J., Kärkelä, T., Heiskanen, K., Reinikainen, M., Rautio, S., Hirvelä, M., and Genoud, G.: On-Line Monitoring of Radiocarbon Emissions in a Nuclear Facility with Cavity Ring-Down Spectroscopy, Analytical Chemistry, 93, 16 096–16 104, https://doi.org/10.1021/acs.analchem.1c03814, 2021.

Levin, I. and Hesshaimer, V.: Radiocarbon – A Unique Tracer of Global Carbon Cycle Dynamics, Radiocarbon, 42, 69–80, https://doi.org/DOI: 10.1017/S0033822200053066, 2000.

Levin, I. and Karstens, U.: Inferring high-resolution fossil fuel CO2 records at continental sites from combined 14CO2 and CO observations, Tellus B, 59, 245–250, https://doi.org/https://doi.org/10.1111/j.1600-0889.2006.00244.x, 2007.

Levin, I., Hammer, S., Kromer, B., and Meinhardt, F.: Radiocarbon observations in atmospheric CO2: Determining fossil fuel CO2 over Europe using Jungfraujoch observations as background, Science of The Total Environment, 391, 211–216, https://doi.org/https://doi.org/10.1016/j.scitotenv.2007.10.019, 2008.

Levin, I., Karstens, U., Eritt, M., Maier, F., Arnold, S., Rzesanke, D., Hammer, S., Ramonet, M., Vítková, G., Conil, S., Heliasz, M., Kubistin, D., and Lindauer, M.: A dedicated flask sampling strategy developed for Integrated Carbon Observation System (ICOS) stations based on CO2 and CO measurements and Stochastic Time-Inverted Lagrangian Transport (STILT) footprint modelling, Atmos. Chem. Phys., 20, 11 161–11 180, https://doi.org/10.5194/acp-20-11161-2020, 2020.

Mahadevan, P., Wofsy, S. C., Matross, D. M., Xiao, X., Dunn, A. L., Lin, J. C., Gerbig, C., Munger, J. W., Chow, V. Y., and Gottlieb, E. W.: A satellite-based biosphere parameterization for net ecosystem CO2 exchange: Vegetation Photosynthesis and Respiration Model (VPRM), Global Biogeochemical Cycles, 22, https://doi.org/https://doi.org/10.1029/2006GB002735, 2008.

Miller, J. B., Lehman, S. J., Montzka, S. A., Sweeney, C., Miller, B. R., Karion, A., Wolak, C., Dlugokencky, E. J., Southon, J., Turnbull, J. C., and Tans, P. P.: Linking emissions of fossil fuel CO2 and other anthropogenic trace gases using atmospheric 14CO2, Journal of Geophysical Research: Atmospheres, 117, https://doi.org/https://doi.org/10.1029/2011JD017048, 2012.

Monteil, G. and Scholze, M.: Regional CO2 inversions with LUMIA, the Lund University Modular Inversion Algorithm, v1.0, Geosci. Model Dev., 14, 3383–3406, https://doi.org/10.5194/gmd-14-3383-2021, 2021.

Monteil, G., Broquet, G., Scholze, M., Lang, M., Karstens, U., Gerbig, C., Koch, F.-T., Smith, N. E., Thompson, R. L., Luijkx, I. T., White, E., Meesters, A., Ciais, P., Ganesan, A. L., Manning, A., Mischurow, M., Peters, W., Peylin, P., Tarniewicz, J., Rigby, M., Rödenbeck, C., Vermeulen, A., and Walton, E. M.: The regional European atmospheric transport inversion comparison, EUROCOM: first results on European-wide terrestrial carbon fluxes for the period 2006–2015, Atmos. Chem. Phys., 20, 12 063–12 091, https://doi.org/10.5194/acp-20-12063-2020, 2020.

Naegler, T. and Levin, I.: Closing the global radiocarbon budget 1945–2005, Journal of Geophysical Research: Atmospheres, 111, https://doi.org/https://doi.org/10.1029/2005JD006758, 2006.

Newman, S., Jeong, S., Fischer, M. L., Xu, X., Haman, C. L., Lefer, B., Alvarez, S., Rappenglueck, B., Kort, E. A., Andrews, A. E., Peischl, J., Gurney, K. R., Miller, C. E., and Yung, Y. L.: Diurnal tracking of anthropogenic CO2 emissions in the Los Angeles basin megacity during spring 2010, Atmos. Chem. Phys., 13, 4359–4372, https://doi.org/10.5194/acp-13-4359-2013, 2013.

Oda, T. and Maksyutov, S.: ODIAC Fossil Fuel CO2 Emissions Dataset (Version name: ODIAC2020b), https://doi.org/10.17595/20170411.001, 2020.

Oda, T., Maksyutov, S., and Andres, R. J.: The Open-source Data Inventory for Anthropogenic CO2, version 2016 (ODIAC2016): a global monthly fossil fuel CO2 gridded emissions data product for tracer transport simulations and surface flux inversions, Earth Syst. Sci. Data, 10, 87–107, https://doi.org/10.5194/essd-10-87-2018, 2018.

Pickers, P. A., Manning, A. C., Le Quéré, C., Forster, G. L., Luijkx, I. T., Gerbig, C., Fleming, L. S., and Sturges, W. T.: Novel quantification of regional fossil fuel CO2 reductions during COVID-19 lockdowns using atmospheric oxygen measurements, Science Advances, 8, eabl9250, https://doi.org/10.1126/sciadv.abl9250, 2022.

Pisso, I., Sollum, E., Grythe, H., Kristiansen, N. I., Cassiani, M., Eckhardt, S., Arnold, D., Morton, D., Thompson, R. L., Groot Zwaaftink, C. D., Evangeliou, N., Sodemann, H., Haimberger, L., Henne, S., Brunner, D., Burkhart, J. F., Fouilloux, A., Brioude, J., Philipp, A., Seibert, P., and Stohl, A.: The Lagrangian particle dispersion model FLEXPART version 10.4, Geosci. Model Dev., 12, 4955–4997, https://doi.org/10.5194/gmd-12-4955-2019, 2019.

https://doi.org/10.5194/egusphere-2023-2215
Preprint. Discussion started: 17 October 2023

Rayner, P. J., Michalak, A. M., and Chevallier, F.: Fundamentals of data assimilation applied to biogeochemistry, Atmos. Chem. Phys., 19, 13 911–13 932, https://doi.org/10.5194/acp-19-13911-2019, 2019.

Rödenbeck, C., Gerbig, C., Trusilova, K., and Heimann, M.: A two-step scheme for high-resolution regional atmospheric trace gas inversions based on independent models, Atmos. Chem. Phys., 9, 5331–5342, https://doi.org/10.5194/acp-9-5331-2009, 2009.

Rödenbeck, C., Keeling, R. F., Bakker, D. C. E., Metzl, N., Olsen, A., Sabine, C., and Heimann, M.: Global surface-ocean pCO2 and sea–air CO2 flux variability from an observation-driven ocean mixed-layer scheme, Ocean Sci., 9, 193–216, https://doi.org/10.5194/os-9-193-2013, 2013.

Scholze, M., Kaplan, J. O., Knorr, W., and Heimann, M.: Climate and interannual variability of the atmosphere-biosphere 13CO2 flux, Geophysical Research Letters, 30, https://doi.org/https://doi.org/10.1029/2002GL015631, 2003.

Scholze, M., Buchwitz, M., Dorigo, W., Guanter, L., and Quegan, S.: Reviews and syntheses: Systematic Earth observations for use in terrestrial carbon cycle data assimilation systems, Biogeosciences, 14, 3401–3429, https://doi.org/10.5194/bg-14-3401-2017, 2017.

Shiga, Y. P., Michalak, A. M., Gourdji, S. M., Mueller, K. L., and Yadav, V.: Detecting fossil fuel emissions patterns from subcontinental regions using North American in situ CO2 measurements, Geophysical Research Letters, 41, 4381–4388, https://doi.org/https://doi.org/10.1002/2014GL059684, 2014.

Smith, B., Wårlind, D., Arneth, A., Hickler, T., Leadley, P., Siltberg, J., and Zaehle, S.: Implications of incorporating N cycling and N limitations on primary production in an individual-based dynamic vegetation model, Biogeosciences, 11, 2027–2054, https://doi.org/10.5194/bg-11-2027-2014, 2014.

Solazzo, E., Crippa, M., Guizzardi, D., Muntean, M., Choulga, M., and Janssens-Maenhout, G.: Uncertainties in the Emissions Database for Global Atmospheric Research (EDGAR) emission inventory of greenhouse gases, Atmos. Chem. Phys., 21, 5655–5683, https://doi.org/10.5194/acp-21-5655-2021, 2021.

Steinbach, J., Gerbig, C., Rödenbeck, C., Karstens, U., Minejima, C., and Mukai, H.: The CO₂ release and Oxygen uptake from Fossil Fuel Emission Estimate (COFFEE) dataset: effects from varying oxidative ratios, Atmos. Chem. Phys., 11, 6855–6870, https://doi.org/10.5194/acp-11-6855-2011, 2011.

Stuiver, M. and Polach, H. A.: Discussion Reporting of 14C Data, Radiocarbon, 19, 355–363, https://doi.org/DOI: 10.1017/S0033822200003672, 1977.

Suess, H. E.: Radiocarbon Concentration in Modern Wood, Science, 122, 415–417, https://doi.org/10.1126/science.122.3166.415.b, 1955.

Tans, P. P., De Jong, A. F. M., and Mook, W. G.: Natural atmospheric 14C variation and the Suess effect, Nature, 280, 826–828, https://doi.org/10.1038/280826a0, 1979.

Thompson, R. L., Broquet, G., Gerbig, C., Koch, T., Lang, M., Monteil, G., Munassar, S., Nickless, A., Scholze, M., Ramonet, M., Karstens, U., van Schaik, E., Wu, Z., and Rödenbeck, C.: Changes in net ecosystem exchange over Europe during the 2018 drought based on atmospheric observations, Philosophical Transactions of the Royal Society B: Biological Sciences, 375, 20190 512, https://doi.org/10.1098/rstb.2019.0512, 2020.

Trumbore, S. E., Sierra, C. A., and Hicks Pries, C. E.: Radiocarbon Nomenclature, Theory, Models, and Interpretation: Measuring Age, Determining Cycling Rates, and Tracing Source Pools, in: Radiocarbon and Climate Change: Mechanisms, Applications and Laboratory Techniques, edited by Schuur, E. A. G., Druffel, E., and Trumbore, S. E., pp. 45–82, Springer International Publishing, Cham, https://doi.org/10.1007/978-3-319-25643-6_3, 2016.

https://doi.org/10.5194/egusphere-2023-2215
Preprint. Discussion started: 17 October 2023

Turnbull, J., Rayner, P., Miller, J., Naegler, T., Ciais, P., and Cozic, A.: On the use of 14CO2 as a tracer for fossil fuel CO2: Quantifying uncertainties using an atmospheric transport model, Journal of Geophysical Research: Atmospheres, 114, https://doi.org/https://doi.org/10.1029/2009JD012308, 2009.

Turnbull, J. C., Keller, E. D., Baisden, T., Brailsford, G., Bromley, T., Norris, M., and Zondervan, A.: Atmospheric measurement of point source fossil CO2 emissions, Atmos. Chem. Phys., 14, 5001–5014, https://doi.org/10.5194/acp-14-5001-2014, 2014.

Turnbull, J. C., Graven, H., and Krakauer, N. Y.: Radiocarbon in the Atmosphere, in: Radiocarbon and Climate Change: Mechanisms, Applications and Laboratory Techniques, edited by Schuur, E. A. G., Druffel, E., and Trumbore, S. E., pp. 83–137, Springer International Publishing, Cham, https://doi.org/10.1007/978-3-319-25643-6_4, 2016.

Turnbull, J. C., Domingues, L. G., and Turton, N.: Dramatic Lockdown Fossil Fuel CO2 Decrease Detected by Citizen Science-Supported Atmospheric Radiocarbon Observations, Environmental Science & Technology, 56, 9882–9890, https://doi.org/10.1021/acs.est.1c07994, 2022.

UNFCCC: THE PARIS AGREEMENT, Tech. rep., https://treaties.un.org/Pages/ViewDetails.aspx?src=TREATY&mtdsg_no=XXVII-7-, 2016.

Vardag, S. N., Gerbig, C., Janssens-Maenhout, G., and Levin, I.: Estimation of continuous anthropogenic CO2: model-based evaluation of CO2, CO, δ13C(CO2) and Δ14C(CO2) tracer methods, Atmos. Chem. Phys., 15, 12 705–12 729, https://doi.org/10.5194/acp-15-12705-2015, 2015.

Vogel, F. R., Levin, I., and Worthy, D. E. J.: Implications for Deriving Regional Fossil Fuel CO2 Estimates from Atmospheric Observations in a Hot Spot of Nuclear Power Plant 14CO2 Emissions, Radiocarbon, 55, 1556–1572, https://doi.org/DOI: 10.1017/S0033822200048487, 2013.

Wang, Y., Broquet, G., Ciais, P., Chevallier, F., Vogel, F., Wu, L., Yin, Y., Wang, R., and Tao, S.: Potential of European 14CO2 observation network to estimate the fossil fuel CO2 emissions via atmospheric inversions, Atmos. Chem. Phys., 18, 4229–4250, https://doi.org/10.5194/acp-18-4229-2018, 2018.

Wang, Y., Broquet, G., Bréon, F.-M., Lespinas, F., Buchwitz, M., Reuter, M., Meijer, Y., Loescher, A., Janssens-Maenhout, G., Zheng, B., and Ciais, P.: PMIF v1.0: assessing the potential of satellite observations to constrain CO2 emissions from large cities and point sources over the globe using synthetic data, Geosci. Model Dev., 13, 5813–5831, https://doi.org/10.5194/gmd-13-5813-2020, 2020.

Wu, Z.: European hourly NEE, GPP and total respiration for 2010-2022 based on LPJ-GUESS (generated in 2023), https://doi.org/10.18160/p52c-1qjm, 2023.

Zazzeri, G., Acuña Yeomans, E., and Graven, H. D.: Global and Regional Emissions of Radiocarbon from Nuclear Power Plants from 1972 to 2016, Radiocarbon, 60, 1067–1081, https://doi.org/DOI: 10.1017/RDC.2018.42, 2018.

Zazzeri, G., Graven, H., Xu, X., Saboya, E., Blyth, L., Manning, A. J., Chawner, H., Wu, D., and Hammer, S.: Radiocarbon Measurements Reveal Underestimated Fossil CH4 and CO2 Emissions in London, Geophysical Research Letters, 50, e2023GL103 834, https://doi.org/https://doi.org/10.1029/2023GL103834, 2023.